UNIVERSITY OF OSLO
Department of geosciences

On the thermally driven large-scale ocean circulation

Master thesis in Geosciences
Meteorology and oceanography

Liv Denstad

01.10.2014

Abstract

The thermally driven large-scale ocean circulation is studied. We obtain a steady state ocean circulation by running the time-dependent, nonlinear model to equilibrium using restoring boundary conditions on surface temperature. This is simulated by MITgcm using a $2^\circ \times 2^\circ$ spherical polar grid.

We examine how this circulation relates to theories of the surface - and the abyssal circulation. These theories include the linear thermocline theory and Stommel and Arons theory.

An important factor in returning the deep water to the surface, is the diapycnal mixing. Why this is important will be discussed. The reasons why and where the deep water upwells, are well debated. We find that positive vertical velocity mainly occurs at the western boundaries, where both the currents in the abyss and at the surface are strong.

The simulated ocean circulation contains many of the observed currents in the world, like the Antarctic Circumpolar Current (ACC), the Kuroshio Current, the Agulhas Current and the Gulf Stream. In addition, the meridional overturning has a realistic strength.

Acknowledgements

I want to thank my supervisor Prof. Joe LaCasce for being an inspiration throughout this study, for arranging and lecturing a crash-course on the thermohaline circulation and for always being available for answering my questions.

Thanks to Gunnar and Anne for helping me getting started with MITgcm, and sharing their technical expertise.

A special thanks to Ada for helping me with the MITgcm setup and for being a great support and problem solver during the several model crashes.

And last, great thanks to my fellow students, my friends and my family for their endless encouragement and support.

Contents

1 Introduction **1**

2 Background theory **3**
2.1 The equations . . . 3
2.2 Driving mechanismes of the ocean circulation . . . 5
2.2.1 Buoyancy . . . 5
2.2.2 Mixing . . . 9
2.2.3 Wind . . . 14
2.3 Analytical solutions . . . 15
2.4 Numerical solutions . . . 17
2.4.1 Horizontal and vertical velocities . . . 17
2.4.2 Topographic effects . . . 18
2.4.3 Meridional overturning circulation . . . 20
2.4.4 Calculating the vertical velocity . . . 21

3 Model description **23**
3.1 MITgcm . . . 23
3.1.1 Computational domain and time stepping . . . 23
3.1.2 Model equations and parameter settings . . . 24

4 Model results **29**
4.1 Vertical structure . . . 29
4.2 Horizontal structure . . . 36
4.2.1 Surface velocities . . . 36
4.2.2 Intermediate-depth circulation . . . 42
4.2.3 Abyssal circulation . . . 43
4.3 Meridional overturning transport . . . 47

5 Summary and discussion **51**
5.1 Comparing model results with theory and observations . . . 51
5.2 Model shortcomings . . . 53

5.2.1 Resolution 53
5.2.2 Salinity and wind 54

6 Conclusions **55**

Appendix A Model parameters **57**

References **61**

List of Figures

2.1 Figure from *Stommel and Arons* (1959): Circulation pattern in a meridionally bounded ocean with a concentrated source S_0 at North Pole and a uniformly distributed sink Q_0. 8

2.2 Illustration of an area ($A = L_x L_y$) where mass conservation in the area above latitude y ($A' = L_x(L_y - y)$) gives an expression for the strength of the western boundary flow. 10

2.3 Figure from *Mauritzen et al.* (2002): Depth-longitude section of diapycnal diffusivity in the Brazil Basin inferred from velocity microstructure observations. 13

2.4 Figure from *Vallis* (2000): Internal thermocline thickness as a function of vertical diffusivity. 14

2.5 Figure from *LaCasce* (2004): Vertically-averaged vertical velocities for a case with a diffusive viscosity. 17

2.6 Figure from *Marotzke* (1997): Boundary mixing case $k_v = 5 \times 10^{-4} m^2 s^{-1}$. (a) Horizontal velocity at 25-m depth and (b) horizontal velocity at 4250-m depth. 18

2.7 Figure from *Broström* (2008- unpublished results): Surface velocities in a basin with (a) flat bottom and (b) a topographic slope along the boundary. 19

2.8 Figure from *Winton* (1997): Vertically integrated circulation for the BOWL geometry. 20

2.9 Figure from *Wunsch* (2002) and *Stammer et al.* (2002): Meridional overturning circulation in the North Atlantic (units of $10^6 m^3 s^{-1}$). . 22

3.1 Model bathymetry 24

3.2 Sea surface temperature forcing curve 25

3.3 Sea surface temperature forcing on bathymetry map 25

3.4 Figure from *MITgcm* (2014): Three-dimensional staggering of velocity components. 26

4.1 Cross sectional temperature profiles at latitude 41°N for (a) Pacific Ocean and (b) Atlantic Ocean. Averaged over 300 years. 30
4.2 Cross-sectional longitudinal temperature profiles for (a) Pacific Ocean, (b) Atlantic Ocean (c) Indian Ocean and (d) Drake passage, and zonally averaged temperature profiles for (e) Pacific Ocean and (f) Atlantic Ocean. 31
4.3 Crossection at latitude 41°N in the Pacific Ocean showing (a) meridional velocity and (c) zonal velocity and in the Atlantic Ocean showing (b) meridional velocity and (d) zonal velocity. (e) Meridional velocity and (f) zonal velocity at latitude 49°N in the Atlantic Ocean 32
4.4 Locations in (a) Pacific Ocean and (b) Atlantic Ocean, for showing vertical structure of (c)/(e) zonal velocities and (d)/(f) temperature. 33
4.5 Temperature profiles and fitted exponential curve in (a) South Pacific Ocean, (b) South Atlantic Ocean, (c) North Atlantic Ocean and (d) Nordic Sea. 34
4.6 Temperature change with depth in (a) North Atlantic Ocean and (b) South Atlantic Ocean. 36
4.7 Global ocean surface horizontal velocities. 37
4.8 Global sea surface (a) temperatures and (b) vertical velocities (at about 100m), and (c) vertically averaged vertical velocity. 38
4.9 Surface velocities in (a) Atlantic and (b) South Atlantic/ACC. (c) is Figure from *Lumpkin and Johnson* (2013): Mean current speeds from near-surface drifter data with streamlines. 39
4.10 Surface velocities (a) in Pacific Ocean and (b) around South Africa/Agulhas current. 41
4.11 Velocities at intermediate depth in (a) global ocean, (b) Atlantic Ocean and (c) Pacific Ocean. 43
4.11 Abyssal velocities at around 2000 m in (a) global ocean and (b) Pacific Ocean. 45
4.12 Vertical velocities at around 1900 m depth in the Atlantic Ocean. Superimposed are the horizontal velocities at around 2100 m. 46
4.13 Abyssal velocities in Atlantic Ocean at around 3500 m. 47
4.14 Zonally averaged global overturning streamfunction. 48
4.15 Stream function of the zonally integrated overturning circulation in (a) the Atlantic Ocean and (b) the Indo Pacific. 49

5.1 Figure from *Lumpkin and Speer* (2007): Schematic of global overturning circulation. Format adapted from *Schmitz* (1996). 53

List of Tables

3.1 Layer thickness used in model run. Numeric subscript indicates the model level index number. 27

Chapter 1

Introduction

The ocean circulation consists of a range of time- and spatial scales, and these interact with each other. By storing and transporting heat, fresh water and carbon around the globe, the large-scale ocean circulation and meridional overturning are important for determining climate and climate variability on Earth. Radiocarbon measurements suggest the thermohaline circulation overturns the deep water every 600 years (*Toggweiler and Key*, 2003). The strength of the thermohaline circulation is not steady, and varies over long time scales. These variations happen, among others, due to periodic external forcing and non-linear interplay of feedbacks within the climate system (*Ghil*, 2002).

To determine the processes going on in the world's ocean, analytical, numerical and observational methods may be used. Numerical models often include non-linear dynamical interactions and either simplified or realistic bathymetry, while analytical models usually are linearized, with flat bottom. Steady state solutions are explored in order to better understand the physical processes that ultimately determine its mean observed behavior. This may then be used to study the stability of the circulation in response to perturbations (*Huck and Vallis*, 2001).

The continents and bathymetry affects both the horizontal and vertical structure of the flow. The ocean is bounded on 5 of 6 sides by complex topography, and bottom bathymetry impacts the currents by topographic steering, diapycnal mixing processes and by separating the water in different ocean basins.

In this study, we will look at theories trying to explain the steady state ocean circulation, both at the surface and in the abyss. The emphasis will be on the thermally driven ocean circulation, neglecting wind forcing and salinity effects. The main driver is the sun, imposing a meridional temperature gradient on the ocean. An indirect effect of wind and tides, though, is included since these have

been proposed as the main energy sources needed for mixing of densities (*Munk and Wunsch*, 1998).

The regions where sinking of dense water occurs are reasonable well identified, mainly at localized convection sites in the high latitudes, but how the water returns to the surface, however, is well debated. Both wind and turbulent diapycnal mixing have been emphasized as factors needed to close the meridional circulation.

Using MITgcm with realistic bathymetry, we obtain a steady state ocean circulation by running the time-dependent, nonlinear model to equilibrium, forcing it only by restoring boundary conditions on surface temperature. This study explore to answer the following questions; where do the strongest vertical velocities occur? Are the model result consistent with theories? How well does the model simulate the global ocean circulation compared to observations? Does the model produce a realistic strength of the meridional overturning? The assumed value of the eddy vertical diffusivity coefficient will also be discussed.

This study is organized as follows. Chapter 2 presents theory relevant for the large-scale ocean circulation, focusing on the thermally driven circulation. Chapter 3 provides a description of the numerical model used, MITgcm. Chapter 4 contains the model results. A summary and discussion are given in chapter 5, and finally chapter 6 presents the conclusions.

Chapter 2

Background theory

Much of the theory presented in this chapter is based on the books by *Vallis* (2006), *Samelson* (2011) and *Pedlosky* (1996).

2.1 The equations

The governing equations express the fundamental physical principles of conservation of mass, -momentum, -salt and -energy, plus the empirically determined equation of state for seawater. When looking at the large-scale circulation, these equations may be simplified, and the mean effect of small-scale motion is parameterized on the large scale. Such a reduced set is called the planetary geostrophic equations.

The principle of conservation of mass, means that fluid mass is neither created nor destroyed. This is better known as the continuity equation, given by

$$\frac{D\rho}{Dt} + \rho \nabla \cdot \vec{u} = 0, \tag{2.1}$$

The density variations in the ocean are very small, and the density term may be therefore be decomposed into $\rho = \rho_0 + \delta\rho(x, y, z, t)$, where $|\delta\rho| << |\rho_0|$. A moving fluid parcel may therefore be considered to be incompressible, which yields

$$\nabla \cdot \vec{u} = \nabla_H \cdot \vec{u} + \frac{\partial w}{\partial z} = 0. \tag{2.2}$$

This approximation, called the Boussinesq approximation, filters out for example sound waves, which are not important for the large scale ocean circulation.

The three-dimensional momentum equation may be written as

$$\frac{D\vec{u}}{Dt} + f\vec{k} \times \vec{u} = -\frac{1}{\rho}\nabla p - g\vec{k} + \nu\nabla^2\vec{u}, \tag{2.3}$$

where the first term on the left-hand side represent the total derivative of the fluid parcel motion $\left(\frac{D}{Dt} = \frac{\partial}{\partial t} + \vec{u}\cdot\nabla\right)$ and the second term represent the the Coriolis force. The first two terms on the right-hand side represent forcing on the fluid parcel due to pressure and gravity respectively. The third term represents the mean effect of small scale turbulence on the large-scale motion, where ν is called the eddy viscosity. This parametrization of turbulence acts to diffuse the momentum of the large scale flow.

In an ocean with no motion (u = v = w = 0) the momentum equations are reduced to a balance between the vertical pressure gradient and gravity, called the hydrostatic balance. Here, the pressure on a fluid parcel is only increasing with depth due to the weight above it. Having this in mind, the pressure term may be decomposed into a static and a varying part $p = p_0(z) + \tilde{p}(x, y, z, t)$, where the horizontally averaged pressure at each height may be linked to the standard density by

$$\frac{dp_0}{dz} = -\rho_0 g. \tag{2.4}$$

By inserting the pressure and density decompositions and utilizing equation (2.4), (2.3) may be written as

$$\begin{aligned}\frac{D\vec{u}}{Dt} + f\vec{k} \times \vec{u} &= -\frac{1}{\rho_0}\nabla\tilde{p} - \frac{1}{\rho_0}\frac{\partial p_0}{\partial z}\vec{k} - \frac{1}{\rho_0}(\rho_0 + \delta\rho)g\vec{k} + \nu\nabla^2\vec{u} \\ &= -\frac{1}{\rho_0}\nabla\tilde{p} + b\vec{k} + \nu\nabla^2\vec{u},\end{aligned} \tag{2.5}$$

where small quadratic terms have been neglected, and $b = -\frac{g}{\rho_0}\delta\rho$ is called the buoyancy. The vertical component of equation (2.5) may, by use of scaling for large scale motion using that vertical scales are much smaller than horizontal scales, be written as

$$\frac{1}{\rho_0}\frac{\partial\tilde{p}}{\partial z} = b. \tag{2.6}$$

From this we see that also the time and spatial varying part of density and pressure, may be considered to be in hydrostatic balance. The variations of density anomalies in the horizontal, gives a horizontal pressure gradient which is an important factor in driving the ocean circulation. So, with this strict balance in the vertical, the $\frac{Dw}{Dt}$-term is no longer present, and the vertical velocity may instead be

diagnosed by use of the continuity equation (2.2). The rate of change of density is obtained from the thermodynamic equation,

$$\frac{D\rho}{Dt} = J' + \kappa\nabla^2\rho.$$

The right-hand side represents the total rate of heating. The second term is diffusion with κ as the eddy diffusivity coefficient, and the first term is the non-diffusive heating component. In the ocean, the latter mainly occur at the upper surface. Typical values of κ is $500m^2s^{-1}$ in the horizontal and 10^{-5}-$10^{-4}m^2s^{-1}$ in the vertical. This equation is analogous to the buoyancy equation

$$\frac{Db}{Dt} = J + \kappa\nabla^2 b, \tag{2.7}$$

If we only look at the horizontal part of equation (2.5), and assume the acceleration $\frac{D\vec{u}}{Dt}$ is small compared to the Coriolis parameter (meaning a small Rossby number), the equation reduces to

$$f\vec{k} \times \vec{u}_H = -\frac{1}{\rho_0}\nabla_H\tilde{p} + \nu\nabla^2\vec{u}_H. \tag{2.8}$$

Together, the equations (2.2) and (2.6)-(2.8) form the planetary geostrophic equations. These are good approximations when looking at the large scale ocean circulation.

2.2 Driving mechanismes of the ocean circulation

2.2.1 Buoyancy

Most of the solar energy is absorbed in the top 100 m of the ocean, and the strength of the incoming solar radiation is decreasing toward the poles, thus giving a meridional temperature gradient. When water moves polewards, it releases heat to the atmosphere. This leads to convection of dense plumes of water in these high latitude regions.

2.2.1.1 Sverdrup theory

In the interior of the ocean beneath the mixed layer and above the bottom of the ocean, equation (2.8) may be simplified to the geostrophic balance. We then have

$$-fv = -\frac{1}{\rho_0}\frac{\partial\tilde{p}}{\partial x}, \tag{2.9}$$

and

$$fu = -\frac{1}{\rho_0}\frac{\partial \tilde{p}}{\partial y}. \tag{2.10}$$

Differentiating equation (2.9) and equation (2.10) by y and x respectively, and subtracting them gives,

$$\beta v + f\nabla_H \cdot \vec{u} = 0. \tag{2.11}$$

where $\beta \equiv \frac{df}{dy}$. The continuity equation (2.2) then may be inserted, yielding

$$\beta v = f\frac{\partial w}{\partial z}, \tag{2.12}$$

which is the planetary vorticity equation, called the Sverdrup balance. This says that northward interior flow must be accompanied by vortex stretching.

2.2.1.2 Stommel and Arons theory

A theory trying to explain the abyssal circulation is the Stommel and Arons theory (see *Stommel and Arons* (1959)). The abyss is here represented as a single layer of homogeneous fluid, and the circulation is considered to be driven by sinking of thermocline water into it at high latitudes, representing convection. To balance this flow into the abyss, water is assumed to rise uniformly out of it in the rest of the basin.

Integrating the Sverdrup balance (2.12) from the bottom of the abyss ($z = -H$) to the bottom of the thermocline ($z = 0$) gives

$$\int_{-H}^{0} \beta v \, dz = \int_{-H}^{0} f\frac{\partial w}{\partial z} \, dz,$$

$$\beta v(0 - (-H)) = f\left(w_0 - w_{(-H)}\right).$$

The bottom is assumed to be flat, which simplifies this to be

$$\beta v H = f w_0 \rightarrow v = \frac{f w_0}{\beta H}. \tag{2.13}$$

So, looking at equation (2.13), we see that when we have upwelling from the abyss ($w_0 > 0$) the meridional velocity is poleward. At the equator ($f = 0$) the interior flow is zero.

The zonal velocity may be found by first identifying the pressure using equation (2.9),

$$\begin{aligned}\int_x^{x_e} \frac{\partial \tilde{p}}{\partial x}\, dx = -\tilde{p}(x) &= \int_x^{x_e} \rho_0 f v\, dx \\ &= \int_x^{x_e} \rho_0 \frac{f^2 w_0}{\beta H}\, dx \\ &= \rho_0 \frac{f^2 w_0}{\beta H}(x_e - x),\end{aligned} \tag{2.14}$$

$$\rightarrow \tilde{p}(x) = -\rho_0 \frac{f^2 w_0}{\beta H}(x_e - x), \tag{2.15}$$

where the boundary condition of no flow into the eastern boundary ($\tilde{p}(x_e) = const. = 0$) has been used.

Then the geostrophic zonal velocity may be found through the use of equation (2.10)

$$\begin{aligned}u &= -\frac{1}{f\rho_0}\frac{\partial \tilde{p}}{\partial y} \\ &= \frac{w_0}{fH\beta}(x_e - x)\frac{\partial f^2}{\partial y} \\ &= \frac{2w_0}{H}(x_e - x).\end{aligned} \tag{2.16}$$

So, the interior abyssal flow is poleward and eastward. Figure 2.1 shows an illustration of this. Due to northward flow in the abyss interior, a western boundary current must be introduced to satisfy mass conservation. In this region the geostrophic Sverdrup balance no longer applies, and is the only region in this model where meridional flow from one hemisphere to the other can happen.

Also, noticing that by adding a bottom Ekman layer to the momentum equations, that eventually would remove the energy supplied, and parameterizing this in term of the velocity, we get

$$\beta v = f\frac{\partial w}{\partial z} - r\zeta, \tag{2.17}$$

where $r\zeta$ represents the friction term, and $\zeta = \frac{\partial v}{\partial x} - \frac{\partial u}{\partial y}$. Integrating this in the vertical,

$$\beta H v = f w_0 - H r\zeta \tag{2.18}$$

$$\beta v = \frac{f}{H} w_0 - r\zeta \tag{2.19}$$

By making $f \to f_0$, the horizontal momentum equations (2.9)-(2.10) may be written as a streamfunction

$$v = \frac{1}{\rho_0 f_0}\frac{\partial p}{\partial x} = \frac{\partial \psi}{\partial x} \text{ and } u = -\frac{1}{\rho_0 f_0}\frac{\partial p}{\partial y} = -\frac{\partial \psi}{\partial y}. \tag{2.20}$$

Then equation (2.19) may be written

$$\beta \frac{\partial \psi}{\partial x} = \frac{f}{H} w_0 - r\nabla^2 \psi. \tag{2.21}$$

This equation is similar to the western boundary current triggered by wind stress, namely the famous Sverdrup relation,

$$\beta \frac{\partial \psi}{\partial x} = \frac{1}{\rho_0 H} \vec{k} \cdot \nabla \times \vec{\tau} - r\nabla^2 \psi. \tag{2.22}$$

Thus, Stommel and Arons assumes a western boundary current. How strong is this?

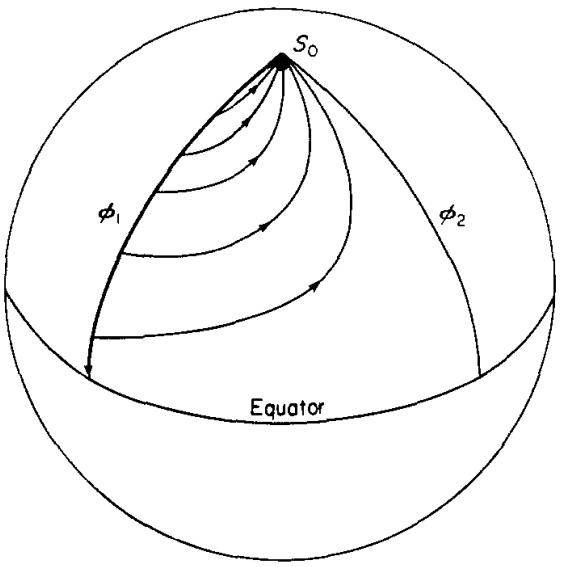

Figure 2.1: Figure from *Stommel and Arons* (1959): Circulation pattern in a meridionally bounded ocean with a concentrated source S_0 at North Pole and a uniformly distributed sink Q_0, that is $Q_0 = \frac{S_0}{A}$ where A is the area of the domain.

If we look at an area above latitudeline y, see Figure 2.2, mass conservation in this area gives

$$S + \int_0^{L_x} vH\,dx - T_w - \int_0^{L_x}\int_y^{L_y} w_0\,dxdy = 0. \tag{2.23}$$

where the two first terms on the left-hand side represent flow into the domain ($A' = L_x(L_y - y)$). S is the strength of the source from the thermocline and $\int_0^{L_x} vH\,dx$ is the poleward interior transport. The terms on the right-hand side represent flow out of the domain A' where T_w is the western boundary transport (positive moving equatorwards) and $\int_0^{L_x}\int_y^{L_y} w_0\,dxdy$ is the integrated upwelling. By using that $w_0 = \frac{S}{A} = \frac{S}{L_x L_y}$, since upwelling is assumed distributed equally over the whole domain, and also using equation (2.13) for the meridional velocity, we may write

$$\begin{aligned} T_w &= -w_0 L_x(L_y - y) + \frac{f w_0 L_x}{\beta} + S \\ &= -\frac{S L_x(L_y - y)}{L_x L_y} + \frac{f S L_x}{\beta L_x L_y} + S \\ &= S\left(-1 + \frac{y}{L_y} + \frac{f_0 + \beta y}{\beta L_y} + 1\right) \\ &= S\left(\frac{2y}{L_y} + \frac{f_0}{\beta L_y}\right). \end{aligned} \tag{2.24}$$

We see from equation (2.24) that the western boundary flow is always equatorwards and strongest near the source, so as it moves towards the equator it loses mass to the interior flow. As mentioned, Stommel and Arons assumed the upwelling from the abyss to be constant a priori. The western boundary current are then, on the basis of this, determined to close the circulation. So, this assumption impacts the whole flow.

2.2.2 Mixing

As pointed out by many, the upwelling is not a given constant, but acts among others as a consequence of diapycnal diffusivity. This diffusivity is needed for the flow to be across isopycnals, as seen by equation (2.7). Studies have shown that this diapycnal diffusivity is not uniform, but depends on geographical location (*Munk and Wunsch*, 1998). But, why is mixing important for the deep circulation?

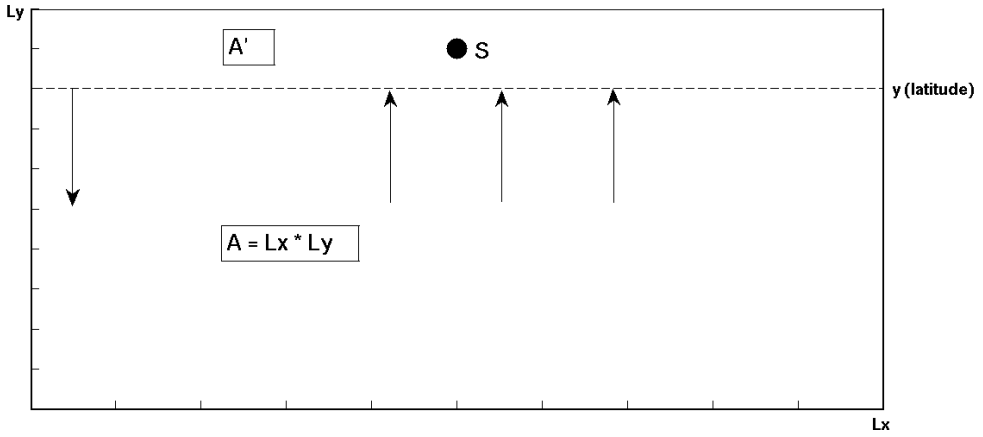

Figure 2.2: Illustration of an area ($A = L_x L_y$) where mass conservation in the area above latitude y ($A' = L_x(L_y - y)$) gives an expression for the strength of the western boundary flow.

2.2.2.1 Sandström's theorem

Sandström's theorem is based on energy conservation. By use of equation (2.5) we may write

$$\vec{u} \cdot \left[\frac{\partial \vec{u}}{\partial t} + \left(\vec{\omega} + f\vec{k} \right) \times \vec{u} = -\nabla\Theta + b\vec{k} + \nu\nabla^2\vec{u} \right], \tag{2.25}$$

where $\Theta = \frac{p}{\rho_0} + \frac{1}{2}|\vec{u}^2|$ and $\vec{\omega} = \nabla \times \vec{u}$. This gives

$$\frac{\partial}{\partial t}\frac{1}{2}|\vec{u}^2| = -\vec{u} \cdot \nabla\Theta + wb + \nu\vec{u} \cdot \nabla^2\vec{u}. \tag{2.26}$$

We see that the coriolis term drops out of the energy equation, since this only changes the flow direction and not the kinetic energy. So, this is the balance of kinetic energy. The sources or sinks of kinetic energy are work done by advection of pressure gradients (first term on right-hand side), conversion between kinetic and potential energy (second term on right-hand side) and dissipation by viscous forces (last term on right-hand side). Integrated over a closed ocean basin volume, the first term on the right-hand side of equation (2.26) will drop out since there are no flow out of the basin boundaries. The third term on right-hand side may by using vector identities be written as

$$\begin{aligned} \nu\vec{u} \cdot \nabla^2\vec{u} &= \nu\vec{u} \cdot (\nabla(\nabla \cdot \vec{u}) - \nabla \times (\nabla \times \vec{u})) \\ &= \nu\vec{u} \cdot (-\nabla \times \vec{\omega}) \\ &= \nu \left(-\vec{\omega}(\nabla \times \vec{u}) + \nabla(\vec{\omega} \times \vec{u}) \right), \end{aligned} \tag{2.27}$$

Integrated over a closed ocean basin volume, this becomes

$$\begin{aligned}\iiint \nu\vec{u}\cdot\nabla^2\vec{u}\,dV &= \nu\iiint\left(-\vec{\omega}(\nabla\times\vec{u})+\nabla(\vec{\omega}\times\vec{u})\right)\,dV\\ &= -\nu\iiint|\omega^2|\,dV\\ &= -\epsilon.\end{aligned} \tag{2.28}$$

Equation (2.26) may then be written as

$$\frac{d}{dt}\left\langle\frac{1}{2}|\vec{u}^2|\right\rangle = \langle wb\rangle - \epsilon, \tag{2.29}$$

where the angle brackets denotes a volume integration. We see that ϵ represent the total sink in kinetic energy due to dissipation. By the use of $z\times$ the buoyancy equation (2.7), we may write this as

$$\frac{d}{dt}\left\langle\frac{1}{2}|\vec{u}^2| - bz\right\rangle = -\left\langle z\left(J+\kappa\nabla^2 b\right)\right\rangle - \epsilon. \tag{2.30}$$

If we now look at the steady state circulation $\left(\frac{\partial}{\partial t}=0\right)$ and with no mixing ($\kappa = 0$), equation (2.30) becomes

$$0 = -\langle zJ\rangle - \epsilon \rightarrow \langle zJ\rangle = -\epsilon < 0. \tag{2.31}$$

So, we realize that the non-diffusive heating needs to be anticorrelated with the height for it to be a steady deep circulation with kinetic energy being dissipated. In other words, the heating must happen at lower depths than cooling. Unlike the atmosphere which is heated from the ground, the ocean is both heated and cooled at the surface. But with $\kappa \neq 0$, we get

$$0 = -\left\langle z\left(J+\kappa\nabla^2 b\right)\right\rangle - \epsilon \rightarrow \langle zJ\rangle = -\left\langle z\kappa\nabla^2 b\right\rangle - \epsilon, \tag{2.32}$$

The $\langle zJ\rangle$ term no longer need to be anticorrelated, but depends on the sign and size of the mixing term. Mixing tends to distribute the heat downwards in the lower latitudes, such that the sharp thermal gradients right at the surface decrease.

Thus, in the absence of mechanical forcing that directly may drive the overturning circulation, the existence of a steady deep ocean circulation needs diapycnal mixing. This increases the oceanic potential energy, and inhibits a uniform density in the whole of the abyss. Because warm water must be pushed down and cold water lifted, mixing needs a power source. *Munk and Wunsch* (1998) estimated the global deep water formation rate to be 30 Sv, and from this estimated the power

required to maintain the abyssal stratification to be 2.1 TW. They claim that wind and tidal power are the most important energy sources. As the tides move over rough bathymetry, it has been suggested that some of the energy associated with its horizontal motion is converted to vertically propagating waves carrying energy up into the water column, where they interact and break (*Ledwell et al.*, 2000).

2.2.2.2 The value of κ_v

The thermodynamic equation (2.7) may be approximated by

$$w\frac{\partial b}{\partial z} = \kappa_v \frac{\partial^2 b}{\partial z^2}, \tag{2.33}$$

where it is assumed that vertical advection w and vertical turbulent mixing are the dominant terms, thereby neglecting horizontal advection and horizontal mixing. Equation (2.33) has been much used, in part due to its simplicity. *Munk* (1966) used this advection/diffusion balance, together with observations of the thermocline in the Pacific, and found an average value of $\kappa_v \approx 10^{-4} m^2 s^{-1}$. It was this value that maintained the abyssal stratification against global uniform upwelling of what he calculated to be 25 Sv ($10^6 m^3 s^{-1}$) of deep water formation.

Estimations of diapycnal diffusivities in the interior thermocline, are typically smaller than Munk's. Different tracer release experiments in the interior of the ocean (e.g. (*Ledwell et al.*, 1993)) have found values on the order of $10^{-5} m^2 s^{-1}$, which suggests that the diffusivity is dependent on location. Other observations suggest enhanced boundary mixing, 10 times stronger than in the interior (*Ledwell and Bratkovich*, 1995). There are ridges in all oceans, and some rise to within 2 km of the ocean surface. Examples of stronger mixing occuring near these deep topographic features were presented by *Ledwell et al.* (2000) and *Mauritzen et al.* (2002), see Fig. 2.3.

2.2.2.3 Estimation of the thermocline depth

The surface water at low latitudes are warmer than the water in the abyss, meaning that vertical temperature gradients are present. The depth where the most rapid temperature change occur is called the thermocline. We may use the steady planetary geostrophic equations to estimate the depth of the thermocline. By combining equation (2.6) and the equations (2.9)-(2.10) we obtain the thermal wind balance

$$\frac{\partial \vec{u}}{\partial z} = \frac{1}{f}\vec{k} \times \nabla b. \tag{2.34}$$

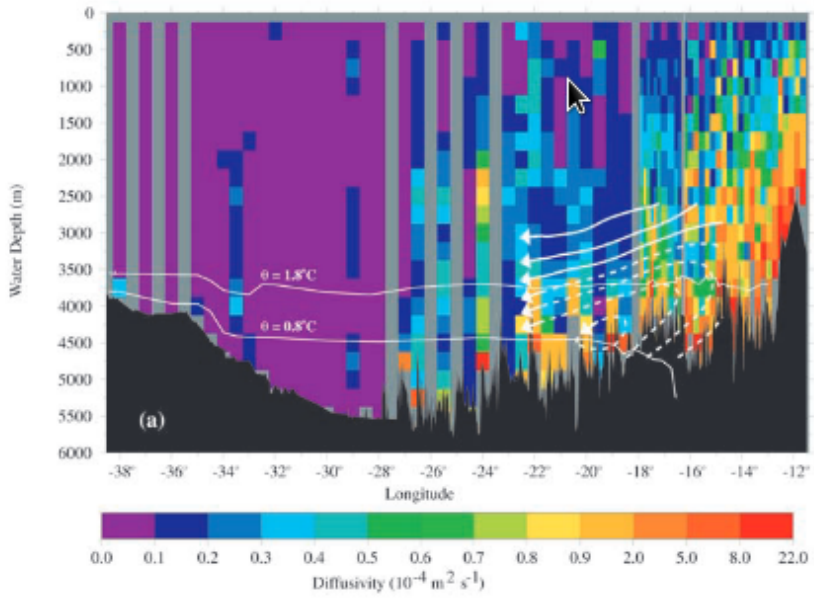

Figure 2.3: Figure from *Mauritzen et al.* (2002): Depth-longitude section of diapycnal diffusivity in the Brazil Basin inferred from velocity microstructure observations, based on observations reported by Polzin et al. [1997], with additional data from a later cruise (*Ledwell et al.*, 2000). Low mixing over smooth topography and high mixing over rough topography.

Scaling this equation gives

$$\frac{U}{H} = \frac{\Delta b}{fL}, \tag{2.35}$$

where H is the depth of the thermocline. The horizontal scales are assumed to be isotropic ($U = V$ and $X = Y = L$). The Sverdrup equation (2.12) scales as

$$\beta U = f\frac{W}{H}, \tag{2.36}$$

We also need to take into account thermodynamics, that is equation (2.33), which scales as

$$\frac{W\Delta b}{H} = \kappa\frac{\Delta b}{H^2} \rightarrow W = \frac{\kappa}{H} \tag{2.37}$$

Combining these three equations gives

$$H = \kappa^{\frac{1}{3}}\left(\frac{f^2 L}{\beta\Delta b}\right)^{\frac{1}{3}}. \tag{2.38}$$

So, in a flow that obeys the planetary geostrophic equations the thermocline depth scales as one-third of the diffusivity. Numerical models have shown to support this scaling, see Figure 2.4.

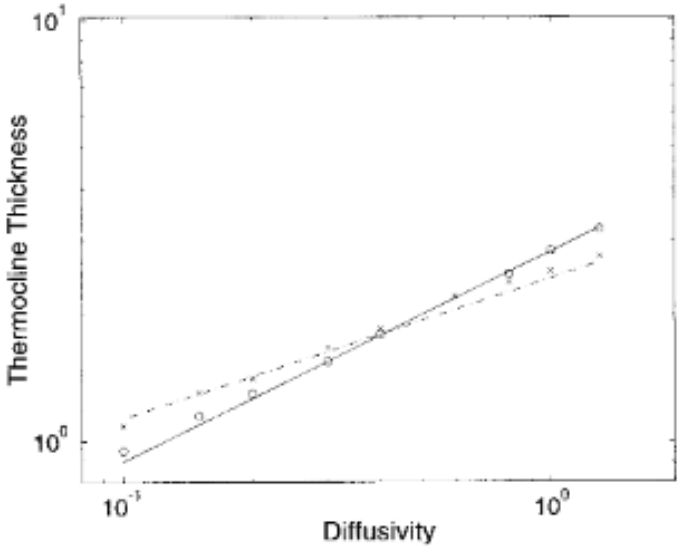

Figure 2.4: Figure from *Vallis* (2000): Internal thermocline thickness as a function of vertical diffusivity, from a single-basin integration in MOM. The circles are from model with wind forcing, and the crosses from model without wind forcing. The solid and dashed lines are, respectively, proportional to $\kappa_v^{1/2}$ and $\kappa_v^{1/3}$.

2.2.3 Wind

Wind systems impact the ocean circulation, and creates gyres and Ekman transport. In the southern hemisphere around 60°, there is no blocking of currents by the continents, so the water may move along the whole latitude circle. This current is named the Antarctic Circumpolar Current (ACC). The meridional Ekman layer transport, due to the surface wind stress which predominantly is in the eastward direction, may be calculated through the relationship

$$\vec{U}_E = \int_{\frac{z}{\delta_E}\to-\infty}^{0} \vec{u}_E \, dz = \frac{1}{\rho_0 f} \left(\tau_\omega^y, -\tau_\omega^x\right) \tag{2.39}$$

where τ_ω is the surface wind stress and δ_E is the boundary layer depth, typically in the upper hundred meters. It is assumed that at depth much larger than this,

the Ekman transport vanishes.

An Ekman vertical velocity may be defined through an incompressibility condition as in (2.2), and by integrating in the vertical this becomes

$$w_E|_{z=0} = -\int_{-\infty}^{0} \nabla \cdot \vec{u}_E dz = -\nabla_h \cdot \vec{U}_E = -W_E, \tag{2.40}$$

where W_E is the "Ekman pumping" defined by

$$W_E = -\frac{1}{\rho_0}\left[\frac{\partial}{\partial x}\left(\frac{\tau_\omega^y}{f}\right) - \frac{\partial}{\partial y}\left(\frac{\tau_\omega^x}{f}\right)\right]. \tag{2.41}$$

The presence of wind stress may therefore cause upwelling of cold deep water, and thereby contribute to the closure of the meridional circulation. *Toggweiler and Samuels* (1998) suggest that a vigorous large-scale circulation persists in a model with a wind-driven ACC in the limit of no vertical mixing. Due to the lack of meridional barriers in the upper 1500 m of the Drake Passage channel, a net geostrophichally balanced flow into the upper channel are not supported. A wind-driven northward Ekman transport then may tend to draw up dense water from deeper levels, which suggest that part of the water sinking in the higher latitudes upwells back to the surface in the Southern Ocean south of the ACC (*Toggweiler and Key*, 2003).

2.3 Analytical solutions

The buoyancy equation (2.7) is still nonlinear, but to simplify an assumption is made, that is

$$b(x, y, z) = \hat{b}(z) + \tilde{b}(x, y, z),$$

where $|\tilde{b}(x, y, z)| \ll |\hat{b}(z)|$. So, the buoyancy term is decomposed into a known part that is only varying in the vertical and a smaller disturbance term.
By use of this, equation (2.7) in steady state may be written as

$$\vec{u} \cdot \nabla\tilde{b} + w\frac{\partial\hat{b}}{\partial z} = J + \kappa\nabla^2\tilde{b} + \kappa_v\frac{\partial^2\hat{b}}{\partial z^2}.$$

The quadratic terms of small disturbance quantities may be neglected, such that

$$w\frac{\partial\hat{b}}{\partial z} = J + \kappa\nabla^2\tilde{b} + \kappa_v\frac{\partial^2\hat{b}}{\partial z^2}. \tag{2.42}$$

If we say $S = \frac{\partial \hat{b}}{\partial z} = const.$, meaning a linear thermocline, and assume no diabatic heating or cooling terms (J = 0) the equation may be reduced to

$$Sw = \kappa_H \nabla_H^2 \tilde{b} + \kappa_v \frac{\partial^2 \tilde{b}}{\partial z^2}, \tag{2.43}$$

so both lateral and vertical diffusion may lead to vertical motion. In the interior the frictional components are small and the Sverdrup relation (2.12) may be used.

By assuming no lateral mixing in this interior domain, which means there are fewer eddies in interior than near the boundaries, using (2.20), and noticing that

$$\frac{\partial \psi}{\partial z} = \frac{1}{\rho_0 f_0} \frac{\partial p}{\partial z} = -\frac{1}{\rho_0 f_0} \rho g = -\frac{1}{f_0} b,$$

equation (2.43) may be written as

$$Sw = \kappa_v f_0 \frac{\partial^3 \psi}{\partial z^3}. \tag{2.44}$$

Inserted in (2.12) this gives

$$\beta \frac{\partial \psi}{\partial x} = \frac{\kappa_v f_0^2}{S} \frac{\partial^4 \psi}{\partial z^4} \tag{2.45}$$

Pedlosky (1969) solved this equation, including both wind and buoyancy forcing, in a square, flat bottom basin and found sinking and upwelling near the boundaries. *LaCasce* (2004) did the same, but by only considering buoyancy forcing, see Figure 2.5. There is an eastward interior surface flow, and there is a stronger western boundary current moving polewards. Upwelling and sinking occurs near the west wall and there is sinking at the north wall . Note that deep convection can not happen in this model, if so, the linear thermocline assumption would be violated.

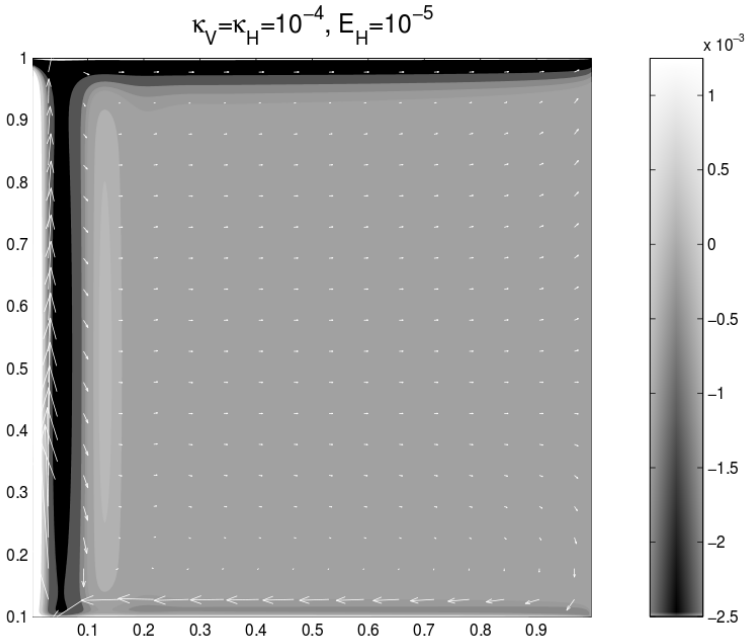

Figure 2.5: Figure from *LaCasce* (2004): Vertically-averaged vertical velocities for a case with a diffusive viscosity. Superimposed are the surface velocities.

2.4 Numerical solutions

Numerical studies, together with analytical models and labaratory experiments, are important for understanding the ocean meridional circulation and its sensitivity to different parameters.

2.4.1 Horizontal and vertical velocities

Marotzke (1997) investigated whether a sensible circulation could be found in a 4°-resolution GCM that assumes vertical mixing only at the margin. The result was quite different than the theory by Stommel and Arons. Wind-forcing is neglected in his model, so there are no wind-induced vertical motion happening in the interior. Also, the bottom is flat.

Figure 2.6 shows the surface and near-bottom horizontal velocities. Compared to Figure 2.1, the interior flow is no longer polewards. Instead the interior velocities are mainly zonal, and meridional flow occurs only in convection regions and at the western boundary. This result is consistent with the Sverdrup balance (2.12), say-

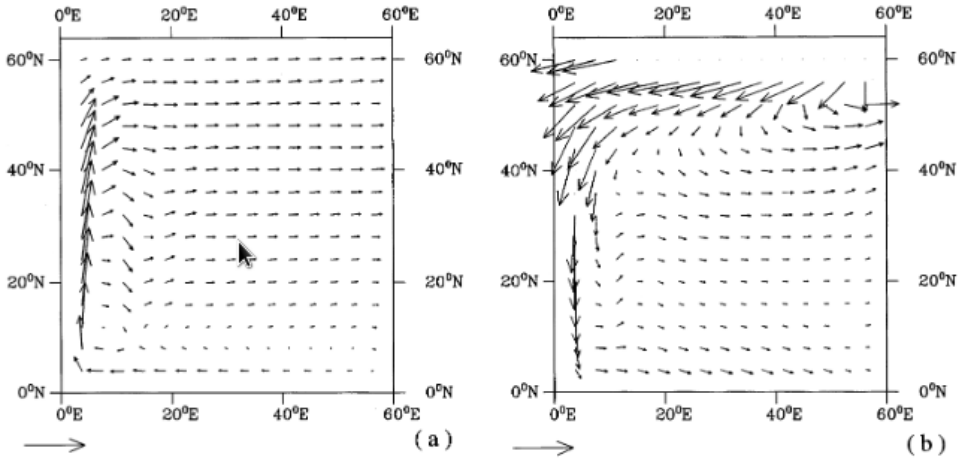

Figure 2.6: Figure from *Marotzke* (1997): Boundary mixing case $k_v = 5 \times 10^{-4} m^2 s^{-1}$. (a) Horizontal velocity at 25-m depth and (b) horizontal velocity at 4250-m depth.

ing that if the upwelling is small or non-existent, the meridional velocity will also be small. His results show upwelling along the western boundary, and downwelling at the upper part of eastern wall, with upwelling underneath extending up to 54°, north of which only downwelling exists. According to his results the mass balance at the eastern boundary mainly is between the zonal and vertical flows.

Comparing his results with a model using uniform diffusivity, *Marotzke* (1997) found that the majority of mixing still happend near the boundaries, but with some increased interior upwelling.

The surface interior flow is very similar to the linear thermocline model, but near the eastern boundary the solution differs. As *Park* (2006) has shown, the numerical simulations of the northern and eastern boundary current are sensitive to the resolution used. As the resolution is increased, the eastern boundary layer is better resolved. So instead of sinking occuring at the eastern margin, a horizontal boundary flow emerges.

2.4.2 Topographic effects

Both the analytical model and numerical models like *Marotzke* (1997) assume a flat bottom. This is not the case in the physical ocean, for example the North Atlantic Current encounters a gradual upward slope as it flows northward toward Iceland and Greenland. How may implementing bathymetry affect the circulation?

Having variable bottom topography, the Sverdrup balance 2.12 integrated over the whole vertical water column becomes

$$\int_{-H}^{0} \beta v = \int f \frac{\partial w}{\partial z} = f w_0 - f w_{-H} = -f w_{-H}, \tag{2.46}$$

where the upwelling from the bottom layer may be written as $w_{-H} = \vec{u} \cdot \nabla h$. So, the flow is no longer only baroclinic, but may have a barotropic component.

By introducing a topographic slope, both *Broström* (2008- unpublished results) and *Winton* (1997) have shown that a northward eastern boundary current emerge, see Fig. 2.7 and Fig. 2.8, forming a cyclonic gyre. The surface velocities on the eastern boundary are now more like what was seen in the analytical model, and the intense downwelling on the eastern boundary is removed.

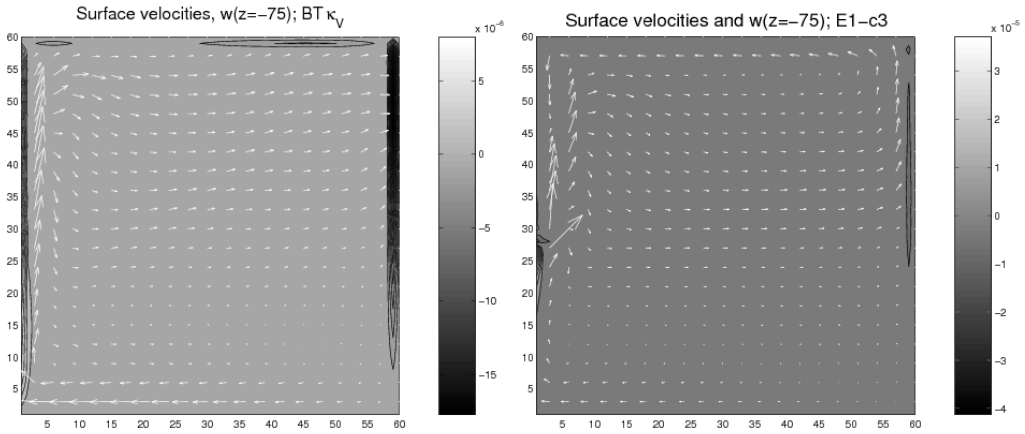

(a) (b)

Figure 2.7: Figure from *Broström* (2008- unpublished results): Surface velocities in a basin with (a) flat bottom and (b) a topographic slope along the boundary.

Thus, with a bottom slope, the cross-shore component of the bottom flow modulates the free surface height through net water column divergence, and builds up a cross-shore pressure gradient. In the rigid-lid models, the energy that would have gone into the free surface deformation instead feed a barotropic mode through bottom pressure torque (*Winton*, 1997).

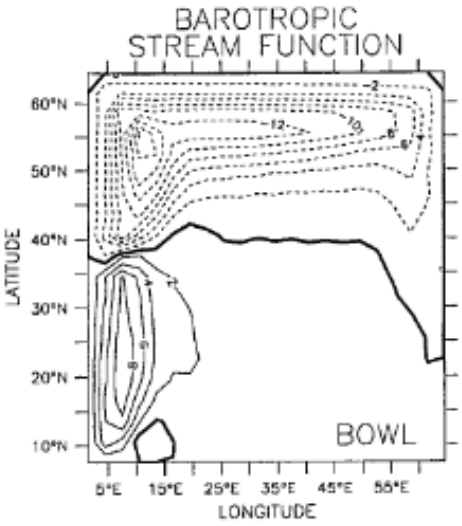

(a)

Figure 2.8: Figure from *Winton* (1997): Vertically integrated circulation for the BOWL geometry.

2.4.3 Meridional overturning circulation

The meridional overturning circulation may be found by integrating the flow zonally. Taking the integral of the continuity equation (2.2) in the x-direction, this becomes

$$\int_{L_w}^{L_e} \frac{\partial u}{\partial x}\, dx + \int_{L_w}^{L_e} \frac{\partial v}{\partial y}\, dx + \int_{L_w}^{L_e} \frac{\partial w}{\partial z}\, dx = 0, \tag{2.47}$$

where both L_e and L_w both depend on y. By using *Leibniz's formula* this becomes

$$u(L_e) - u(L_w) + \frac{\partial}{\partial y}\int_{L_w}^{L_e} v\, dx + v(L_w)\frac{dL_w}{dy} - v(L_e)\frac{dL_e}{dy} + \frac{\partial}{\partial z}\int_{L_w}^{L_e} w\, dx = 0. \tag{2.48}$$

Implementing the boundary conditions of no normal and lateral flow at the boundaries yields

$$\frac{\partial V}{\partial y} + \frac{\partial W}{\partial z} = 0, \tag{2.49}$$

where $V = \int_{L_w}^{L_e} v\, dx$ and $W = \int_{L_w}^{L_e} w\, dx$. Because the zonally integrated velocities are divergence-free they may be written in terms of a streamfunction

$$V = -\frac{\partial \psi}{\partial z} \qquad \text{and} \qquad W = \frac{\partial \psi}{\partial y}. \tag{2.50}$$

For calculation of the streamfunction, we could use both the zonally-averaged meridional velocity - and vertical velocity. The former is often more practical, due to inaccuracy of the vertical velocity, see the next section. Thus,

$$\psi(y, z) = -\int_{-H}^{z} V \, dz, \tag{2.51}$$

where $-H$ and η are the bottom depth and surface height, respectively. While this does not distinguish the boundaries from the interior, it gives an overall view of the strength and depth of sinking and upwelling. Figure 2.9 shows the streamfunction in the North Atlantic by use of a general circulation model constrained to observations (*Wunsch*, 2002). At the high latitudes we see a downward mass flux, associated with regions of heat loss to the atmosphere.

2.4.4 Calculating the vertical velocity

One may calculate w by integration of the continuity equation (2.2),

$$w(z) = w(0) + \int_{z}^{0} \left(\frac{\partial u}{\partial x} + \frac{\partial v}{\partial y} \right) dz. \tag{2.52}$$

So, knowledge of the horizontal divergence is required in determining the vertical velocity. In numerical schemes this is generally calculated by use of finite difference approximations. For example we may write

$$\frac{\partial u}{\partial x} + \frac{\partial v}{\partial y} \approx \frac{u(x_0 + d) - u(x_0 - d)}{2d} + \frac{v(y_0 + d) - u(y_0 - d)}{2d} \tag{2.53}$$

A small error in the calculation of the horizontal velocities, however, may cause a large error in its divergence and thereby the vertical velocities (*Holton*, 2004).

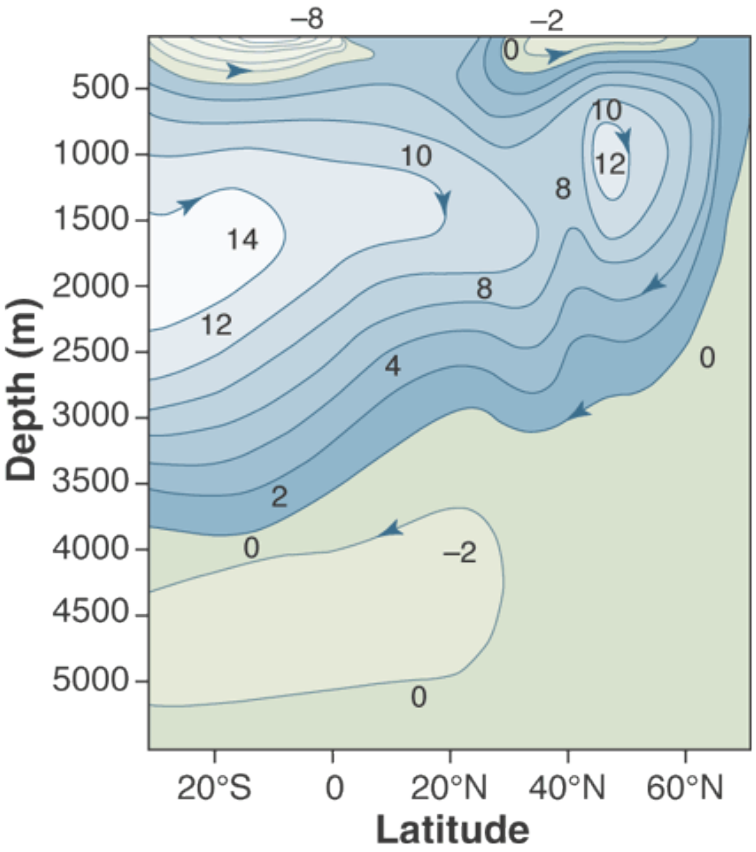

Figure 2.9: Figure from *Wunsch* (2002) and *Stammer et al.* (2002): Meridional overturning circulation in the North Atlantic (units of $10^6 m^3 s^{-1}$). Values comes from a general circulation model constrained to observations.

Chapter 3

Model description

3.1 MITgcm

The ocean circulation is simulated by use of the MIT general circulation model (MITgcm), see *MITgcm* (2014). This model may be used to study the atmosphere and ocean separately, or coupled.

3.1.1 Computational domain and time stepping

The simulation is configured on a $2^\circ \times 2^\circ$ spherical polar grid. Meridionally the model extends from 84°S to 84°N. The model employs height as the vertical coordinate, represented by 24 layers. These are ranging in thickness from about 15 m near the surface to about 950 m at depth, see Table 3.1. This gives a maximum depth of 5665.9 m. The "shaved cell" approach is implemented in the model, such that the bottom cell is a piecewise fit to the bathymetry. The model bathymetry are shown in Figure 3.1a.

The diffusive timescale is given by $T_{diff} \sim \frac{D^2}{\kappa_v} \approx \frac{(5\times10^3)^2 m^2}{10^{-4} m^2 s^{-1}} = 25\times10^{10} s \approx 8000$yrs. But, the advective processes given by $T_{adv} \sim \frac{L}{U} = \frac{10^7 m}{0.02\times10^{-2} m s^{-1}} = 5\times10^{10} s \approx 1500$ yrs can accelerate equilibrium. By use of this, the model was run for 2000 years. At the end of this integration period, the model properties were not changing much and therefore considered being in a steady state. In the analyses of the flow, we averaged over the last 300 years of integration, such that small fluctuations are evened out.

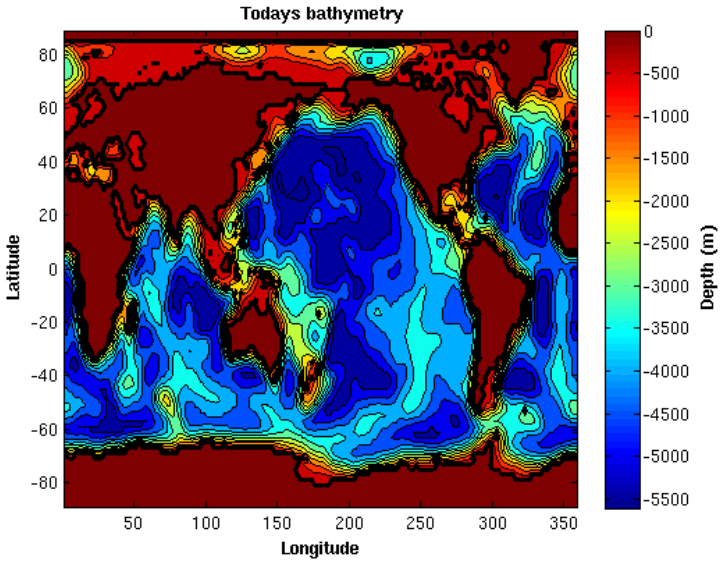

(a)

Figure 3.1: Model bathymetry

3.1.2 Model equations and parameter settings

Since the purpose of this study is to investigate the thermally driven ocean circulation, some realism must be sacrificed. Thus, both wind stress and salinity effects on density are neglected. A sinusoidal varying temperature is imposed at the surface, see Figure 3.2 and 3.3. As a third simplification, seasonality is neglected, meaning the imposed temperature gradient is constant, in this case corresponding to an equinox period.

The model is configured in hydrostatic form with an implicit free surface. So, at each time step the internal pressure is calculated by

$$g\rho_0\eta + \int_{-z}^{0} \delta\rho \, dz = \tilde{p}, \tag{3.1}$$

where η is the sea surface height from the reference level $z = 0$. The model is forced by restoring boundary conditions on surface temperature, that is

$$\mathcal{F}_\theta = -\lambda_\theta(\theta - \theta^*), \tag{3.2}$$

where λ_θ is chosen to produce a restoring time of 30 days, θ is the model calculated potential temperature and θ^* is the externally applied temperature field. Due to ocean currents, the sea surface temperature will deviate from the forcing field.

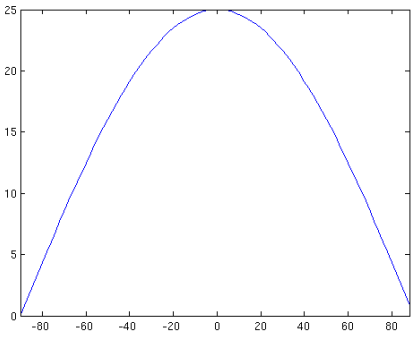

Figure 3.2: Sea surface temperature forcing curve

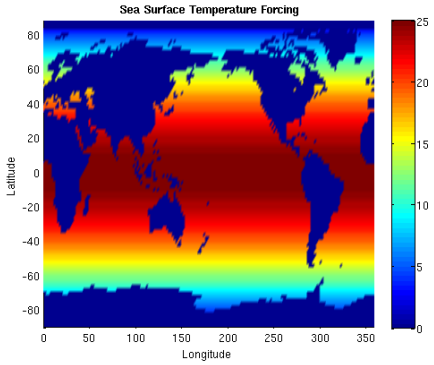

Figure 3.3: Sea surface temperature forcing on bathymetry map

The potential temperature equation solved is thus

$$\frac{D\theta}{Dt} - \nabla_h \cdot K_h \nabla_h \theta - \frac{\partial}{\partial z}\Gamma(K_z)\frac{\partial \theta}{\partial z} = \begin{cases} \mathcal{F}_\theta & \text{(surface).} \\ 0 & \text{(interior).} \end{cases} \tag{3.3}$$

Thermal diffusion is parameterized by a Laplacian operator, ∇^2. Horizontal diffusivity, K_h, is set to $500 m^2 s^{-1}$. Diapycnal mixing is approximated by vertical mixing, K_z, and on the basis of earlier work (e.g. *Munk* (1966)), is set to $10^{-4} m^2 s^{-1}$. When the ocean becomes statically unstable vertical overturning should occur, but due to hydrostatic balance it cannot. Therefore, ocean convection is parameterized with an implicit vertical diffusion. In the case of static instability the vertical diffusivity is increased by $100 m^2 s^{-1}$.

Neglecting wind, the horizontal momentum equations solved are

$$\frac{D\vec{u_H}}{Dt} + f\vec{k} \times \vec{u_H} + \frac{1}{\rho}\nabla_H p' - \nabla_H \cdot A_H \nabla_H \vec{u} - \frac{\partial}{\partial z} A_z \frac{\partial \vec{u_H}}{\partial z} = 0, \tag{3.4}$$

both at the surface and in the interior. Subgrid-scale viscous processes are also represented by a Laplacian operator, where A_H and A_z are the eddy viscosities for the horizontal and vertical directions, respectively. These viscosities are normally considerably larger than the molecular viscosities. The no-slip ($\vec{v} \times \vec{n}$) and the no normal flow condition are used at the lateral walls. The vertical velocity is diagnosed from the continuity equation.

A staggered C-grid is used in stepping forward the momentum equations, see Fig. 3.4a. This assures non-divergence of the flow at all times. See appendix A for further information on parameter settings.

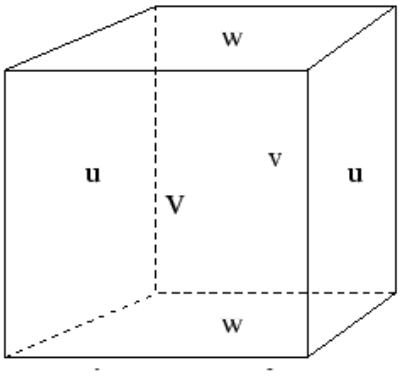

(a)

Figure 3.4: Figure from *MITgcm* (2014): Three-dimensional staggering of velocity components.

Table 3.1: Layer thickness used in model run. Numeric subscript indicates the model level index number.

Layer	Thickness
Δz_1	14.8461
Δz_2	17.7881
Δz_3	21.3130
Δz_4	25.5365
Δz_5	30.5969
Δz_6	36.6601
Δz_7	43.9247
Δz_8	52.6290
Δz_9	63.0581
Δz_{10}	75.5539
Δz_{11}	90.5259
Δz_{12}	108.4648
Δz_{13}	129.9585
Δz_{14}	155.7114
Δz_{15}	186.5677
Δz_{16}	223.5385
Δz_{17}	267.8356
Δz_{18}	320.9107
Δz_{19}	384.5033
Δz_{20}	460.6977
Δz_{21}	551.9909
Δz_{22}	661.3751
Δz_{23}	792.4352
Δz_{24}	949.4666

Chapter 4

Model results

Both the analytical- and the numerical buoyancy driven model discussed previously assumes a square basin and flat bottom. However, we have seen that introducing a bottom slope alter the steady- state circulation. Variable bottom topography exists and since abyssal currents are not vanishing, the overall density structure and ocean circulation would be expected to have some deviations from the flat-bottomed models. How will the ocean circulation look like using a thermally driven numerical model with realistic bathymetry?

4.1 Vertical structure

The model results of the potential temperature distribution at latitude 41°N are shown in Figure 4.1 for the Pacific Ocean and the Atlantic Ocean. Since salinity is neglected, the isentropes are equivalent to isopycnals. Potential temperature is referred to as temperature hereafter. Their surfaces are basically flat, but we see deviations in the upper part of the ocean, mainly near the boundaries. The lowering of the upper ocean isopycnals near the eastern coast is related to sinking.

Figure 4.2a-4.2d is a north-south section showing the distribution of temperature for the same basins, but also including the Indian Ocean and Drake Passage. The places where the isentropes outcrop, are where the deep and intermediate waters are most susceptible to bouyancy forcing at the surface, and are associated with convection sites. This happens at high latitudes, especially in the North Atlantic and in the Southern Ocean. The depth of the thermocline is about 1000 m. The Drake Passage (Fig. 4.2d) extends down to about 3400 m. This region contains sharp meridional temperature gradients. The zonally averaged temperature in the Atlantic (Fig. 4.2f) show the presence of relative warm water in front of the ridge in the northern hemisphere, and colder water behind. The temperature difference

on each side of the sill provides a density gradient that drives the flow of dense water in to the deep North Atlantic.

The energy stored in horizontal variations of the density field is known as available potential energy. If the forcing were to be turned off, this low-density bowl-shaped water floating on top of the denser water would flatten out, converting the available potential energy to kinetic energy, and eventually would be dissipated away (*Toggweiler and Samuels*, 1998).

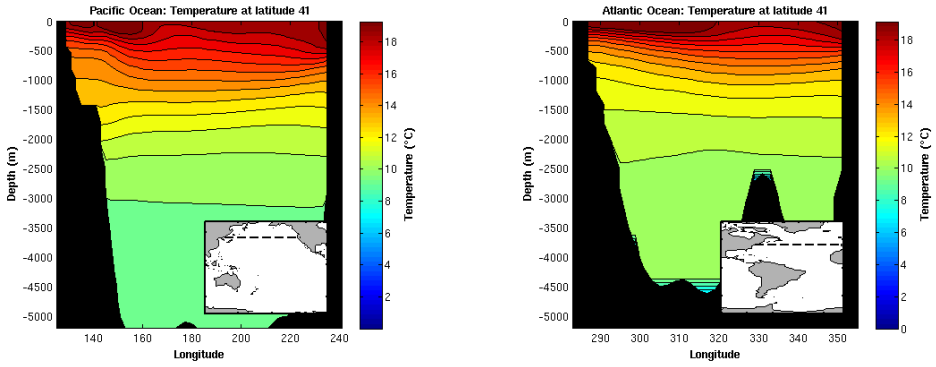

(a) Pacific Ocean (b) Atlantic Ocean

Figure 4.1: Cross sectional temperature profiles at latitude 41°N for (a) Pacific Ocean and (b) Atlantic Ocean. Averaged over 300 years.

The temperature gradients in the horizontal are associated with baroclinic flows from the thermal wind equation (2.34). Figure 4.3 shows meridional and zonal velocities in the Atlantic and Pacific Ocean. In the upper ocean in both basins we see strong northward flow on the western side, and a return flow below. In the Atlantic the flow structure is deeper, and western intensified. The zonal current decreases from west to east, and rises toward the surface.

To look further at the 300 year- averaged profiles of the zonal flow, both near and away from boundaries, we have chosen some locations in the Pacific and the Atlantic Ocean, see Figure 4.4. The northward flowing Atlantic western boundary current spans a depth range from the surface down to $\sim$ 1000 m, carrying with it thermocline- and intermediate-depth temperatures in the range 12-24°C, while in the Pacific it spans down to $\sim$ 600 m. In both ocean basins there is an eastward surface flow in all locations. In the Pacific the zonal flow is close to zero below around 2000 m, while it extends a bit deeper in the Atlantic. The zonal velocities mainly have one zero crossing, occuring at different depths depending on location.

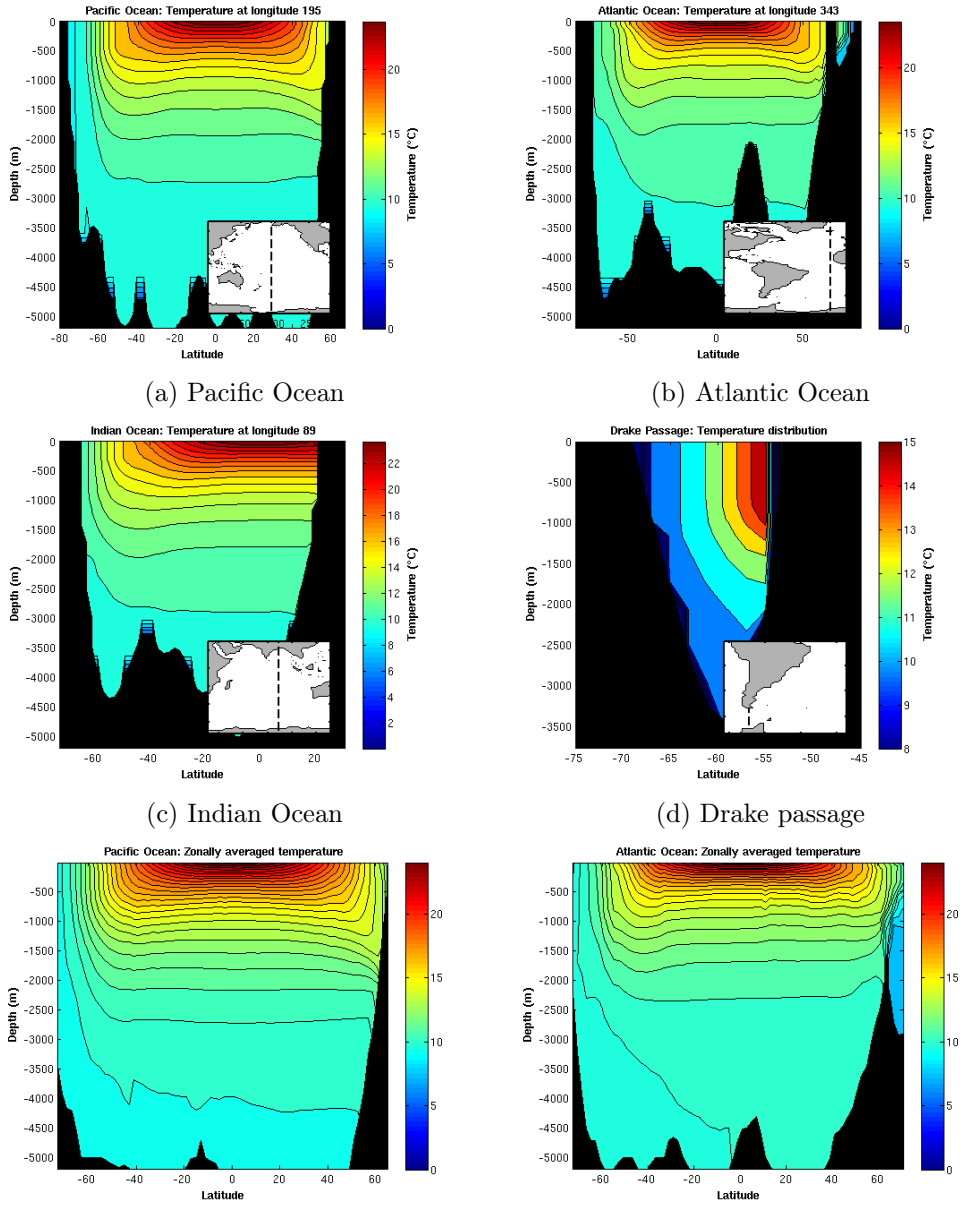

Figure 4.2: Cross-sectional longitudinal temperature profiles for (a) Pacific Ocean, (b) Atlantic Ocean (c) Indian Ocean and (d) Drake passage, and zonally averaged temperature profiles for (e) Pacific Ocean and (f) Atlantic Ocean.

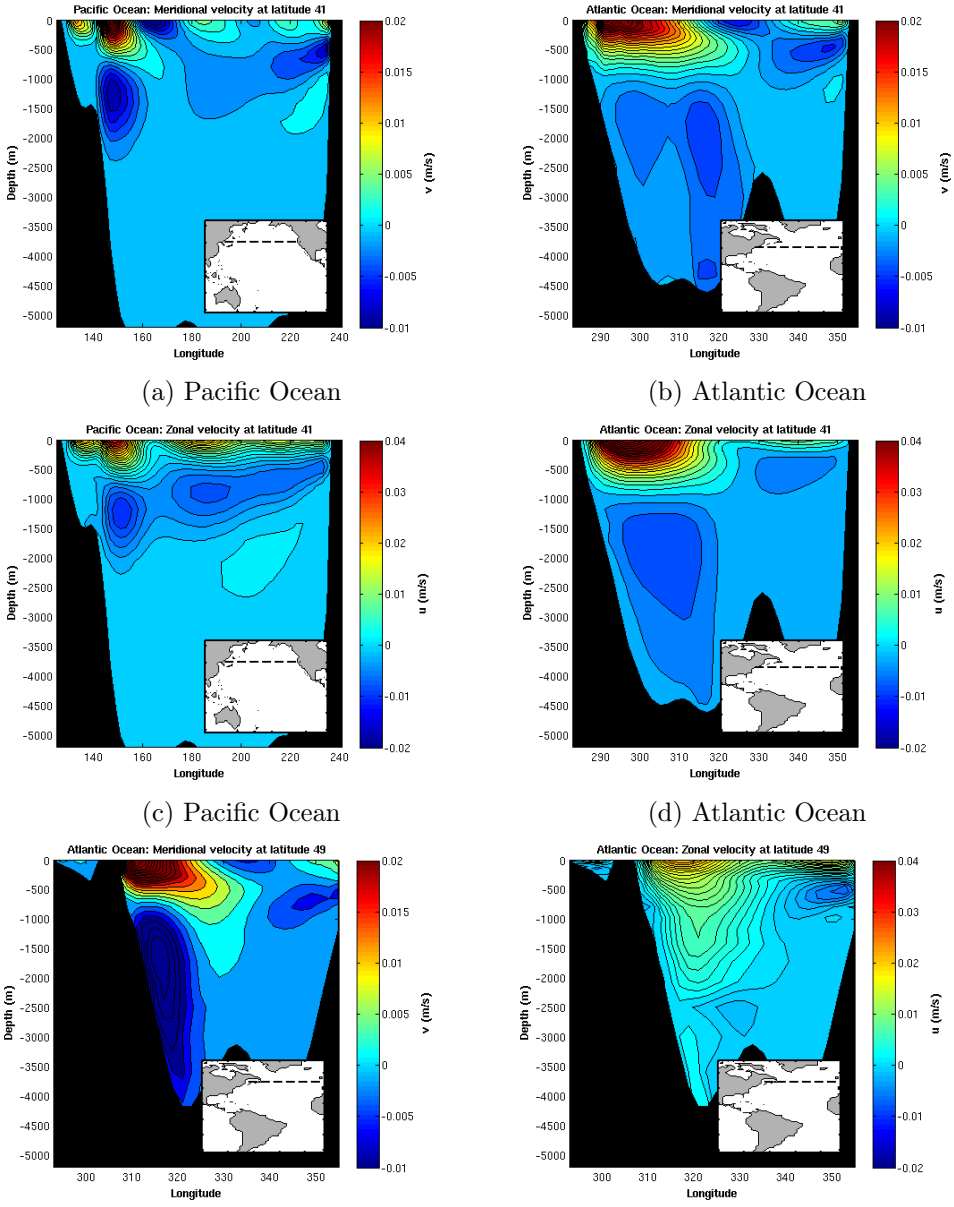

(a) Pacific Ocean

(b) Atlantic Ocean

(c) Pacific Ocean

(d) Atlantic Ocean

(e) Atlantic Ocean

(f) Atlantic Ocean

Figure 4.3: Crossection at latitude 41°N in the Pacific Ocean showing (a) meridional velocity and (c) zonal velocity and in the Atlantic Ocean showing (b) meridional velocity and (d) zonal velocity. (e) Meridional velocity and (f) zonal velocity at latitude 49°N in the Atlantic Ocean

Their structure looks like a baroclinic mode 2 over rough bottom topography, see *LaCasce* (2012), with an eastward flow at the surface and westward below, as in the linear thermocline model. An exception is at latitude 49°N in the Atlantic, also see Fig. 4.3f, where there is a baroclinic mode 1 structure with eastward flow spanning the entire depth.

At the northern most points the temperature is uniform in the top layer due to convection. Moving toward Iceland the ocean becomes shallower, and the baroclinic mode 2 structure is "compressed". A return flow from the Nordic Seas into North Atlantic occurs at around 600 m depth.

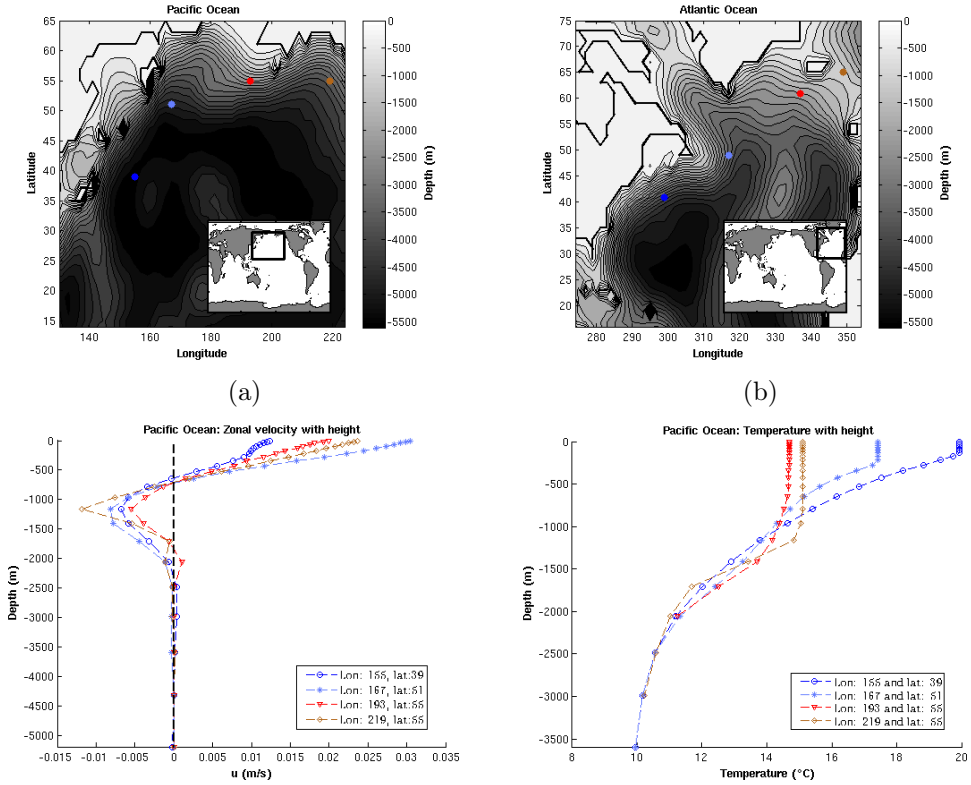

Figure 4.4: Locations in (a) Pacific Ocean and (b) Atlantic Ocean, for showing vertical structure of (c)/(e) zonal velocities and (d)/(f) temperature.

As we have discussed before, the surface waters are warmer than the waters in the abyss. To find an approximately depth of the thermocline, we may fit the

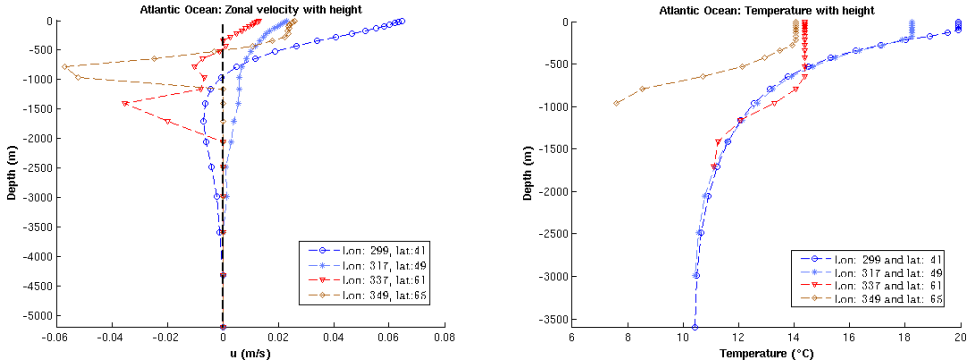

(e) (f)

Figure 4.4: (continued)

temperature height profile to an exponential function,

$$T = (T_T - T_B)\exp(\frac{z}{\delta}) + T_B, \tag{4.1}$$

where T_T is the surface temperature, T_B the bottom temperature and δ is the e-folding depth, considered being the depth of the thermocline. Figure 4.5 shows how well the temperature is fit with an exponential, and in all locations the e-folding depth is around 1000 m, except in the shallow region in the Nordic Seas under the mixed layer.

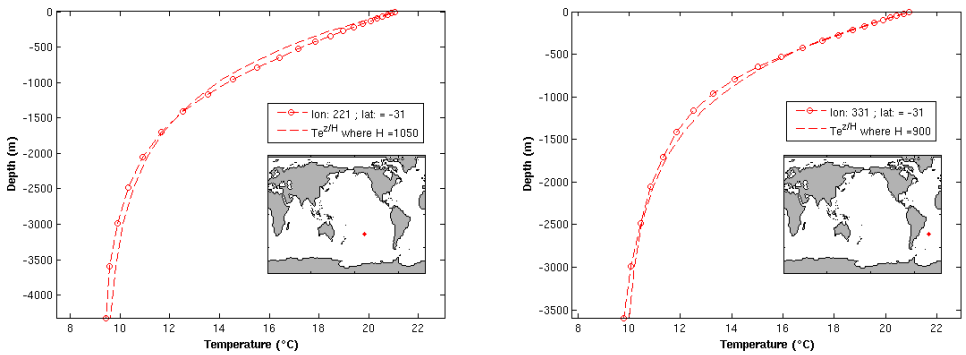

(a) South Pacific (b) South Atlantic

Figure 4.5: Temperature profiles and fitted exponential curve in (a) South Pacific Ocean, (b) South Atlantic Ocean, (c) North Atlantic Ocean and (d) Nordic Sea.

The depth of the thermocline, from scaling the planetary geostrophic equations

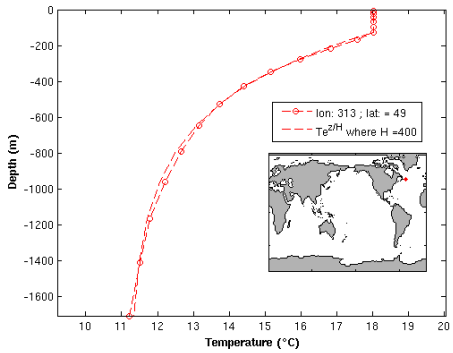

(c) North Atlantic

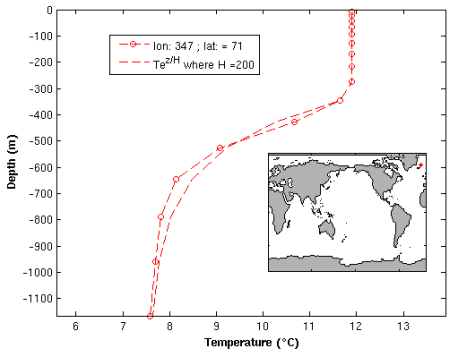

(d) Nordic Sea

Figure 4.5: (continued)

(section 2.2.2.3) is

$$\begin{aligned} H &= \left(10^{-4}\right)^{\frac{1}{3}} \left(\frac{\left(10^{-4}\right)^2 \times 5 \times 10^6}{10^{-11} \times 10 \times 10 \times 10^{-4}} \right)^{\frac{1}{3}} \\ &= \left(10^{-4}\right)^{\frac{1}{3}} \left(\frac{5 \times 10^{-2}}{10^{-13}} \right)^{\frac{1}{3}} \\ &= 5^{\frac{1}{3}} \times 10^{\frac{7}{3}} \\ &\approx 370m. \end{aligned} \tag{4.2}$$

using values relevant for the North Atlantic and the midlatitudes, with $f = 10^{-4}s^{-1}$, $\beta = 10^{-11}m^{-1}s^{-1}$, $L = 5 \times 10^6 m$ and $\Delta b = g\alpha_T \Delta T \rightarrow g = 10ms^{-2}; \alpha_T = 10^{-4}K^{-1}; \Delta T = 10K$, in addition to $\kappa_v = 10^{-4}m^2s^{-1}$ have been used. Comparing the two estimates, we see that $\delta \approx 3H$ in the middle of the ocean basins. At shallower depths in the North Atlantic, more sinking is occuring. This yields an upper mixed layer, squeezing the depth of the thermocline.

As done in *Vallis* (2000), we could define the thermocline thickness as the distance from the surface to the half-maximum of $\frac{\partial T}{\partial z}$. We see from Figure 4.6a that this gives an estimate closer to the scaling. But at other locations (Fig. 4.6b) an estimate is difficult to find.

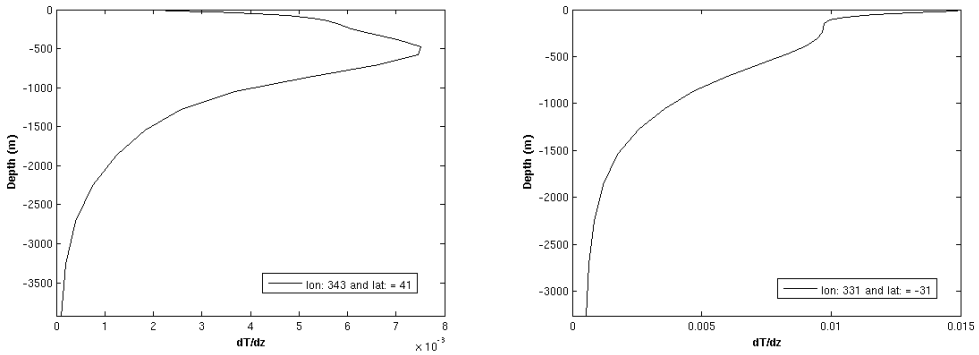

(a) (b)

Figure 4.6: Temperature change with depth in (a) North Atlantic Ocean and (b) South Atlantic Ocean.

4.2 Horizontal structure

4.2.1 Surface velocities

The global surface horizontal velocities are shown in Fig. 4.7a. Many of the major current systems in the world are present. Due to the relative low resolution and the lack of wind, they are smoother and broader than observed. The most striking features are the poleward flowing western boundary currents in the North Atlantic and the Pacific, and the Antarctic Circumpolar Current. As seen from the global temperature distributions in Fig. 4.8a, we see that the western currents transport heat polewards. The interior flow is mostly eastward, due to the near surface meridional temperature gradient. Around the equator there is a weak westward flow. We see that the currents travel the farthest north in the North Atlantic Ocean, yielding warmer sea surface temperatures west of Europe.

Even though mixing is applied over the whole region, not only at the margin, vertical velocities in the oceans' upper layers are far from spatially uniform, and are clearly impacted by topography. The largest vertical velocity amplitudes are found over rough topography and near boundaries (Fig. 4.8b) with typically upwelling on the western - and downwelling on the eastern side of the ocean basins. This resembles the study by *Marotzke* (1997) in a square basin. As discussed earlier, the downwelling on the eastern side may be resolution dependent (*Park*, 2006). Weak positive vertical velocities are also seen around the equator.

Looking more closely at the Atlantic ocean, Fig. 4.9a, we see a relative strong current transporting water northwards along the western boundary, continuing past

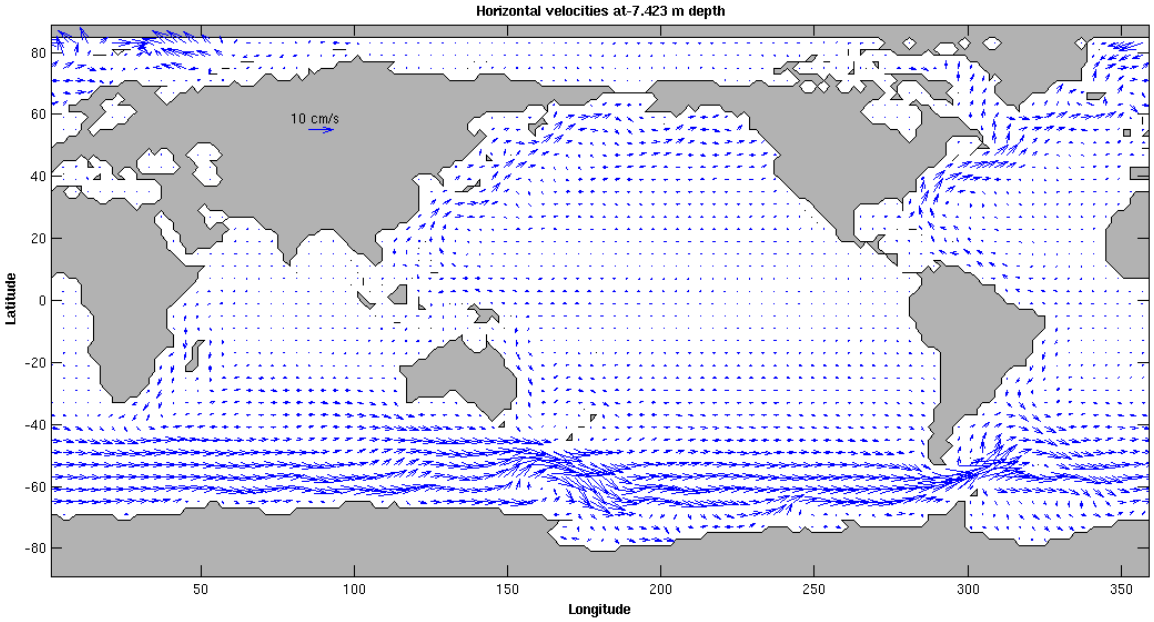

(a)

Figure 4.7: Global ocean surface horizontal velocities.

East of Greenland. This "flooding" from the North Atlantic to the Nordic Seas may seem a bit extreme. Figure 4.9c shows an overview of the surface flow based on observations in the Atlantic. Here, the Gulf stream leaves the coast at Cape Hatteras and flows out to the open sea, where one branch turn southeast later to become part of the Canary Current, while the rest moves further north along western Europe. Also, observations support a cyclonic gyre south of Greenland. These features are not well represented in our model, and could be expected by the neglect of windstress, which is known to drive cyclonic circulation in the subpolar ocean and anticyclonic circulation in the subtropical gyre.

In the South Atlantic, Fig. 4.9b, we notice the Brazil current, moving southwards eventually joining the ACC. Some of the water that is flowing through Drake Passage, between the tip of South America and the Antarctic Peninsula, takes a northward excursion along the eastern side of South America, meeting the Brazil current, before returning south again. This is also seen in Figure 4.9c, and may be caused by topography in this area.

The Drake Passage enables water to flow continuously eastward, encircling Antarctica. The ACC is the largest current in the global ocean, and is a pathway for water to be exhanged between the ocean basins. Its presence is important in

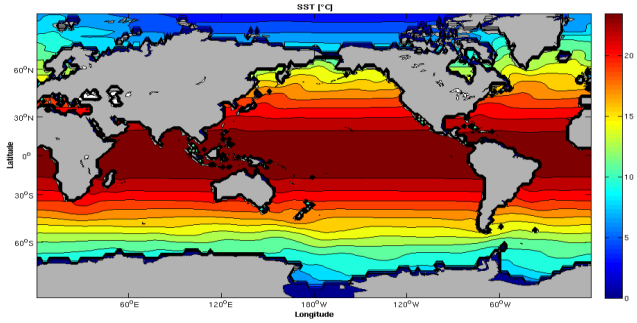

(a)

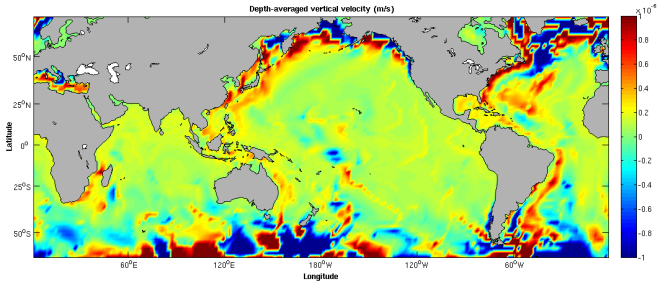

(b)

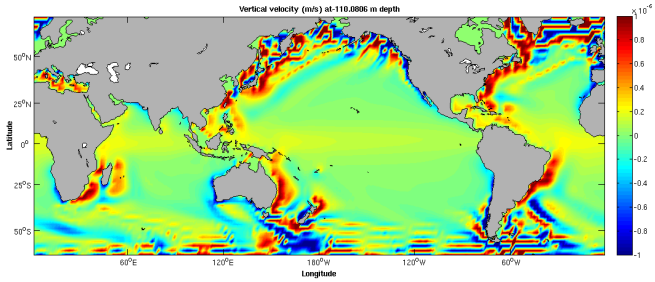

(c)

Figure 4.8: Global sea surface (a) temperatures and (b) vertical velocities (at about 100m), and (c) vertically averaged vertical velocity.

determining the ocean circulation ((*Nowlin Jr et al.*, 1977),(*Nowlin and Klinck*, 1986),(*LaCasce and Isachsen*, 2010)) and climate. It acts as a dynamical barrier to meridional transport, thus isolating the water around Antarctic and contribute to its colder climatic conditions. To get an estimate of the strength of the ACC we integrate the zonal velocities across this passage (see dashed line in Figure 4.9b),

$$\int_{-H}^{0} \int_{ANP}^{SA} u \, dydz \approx 133 \, Sv \, [10^6 m^3 s^{-1}] \tag{4.3}$$

Observations estimate the average yearlong absolute transport through Drake Pas-

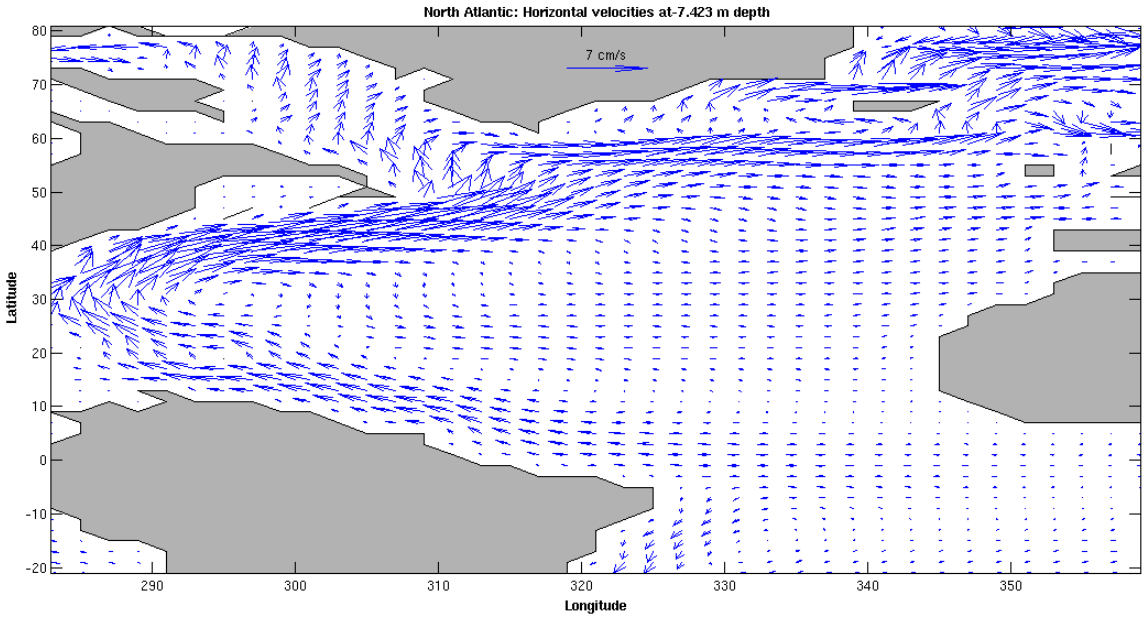

(a)

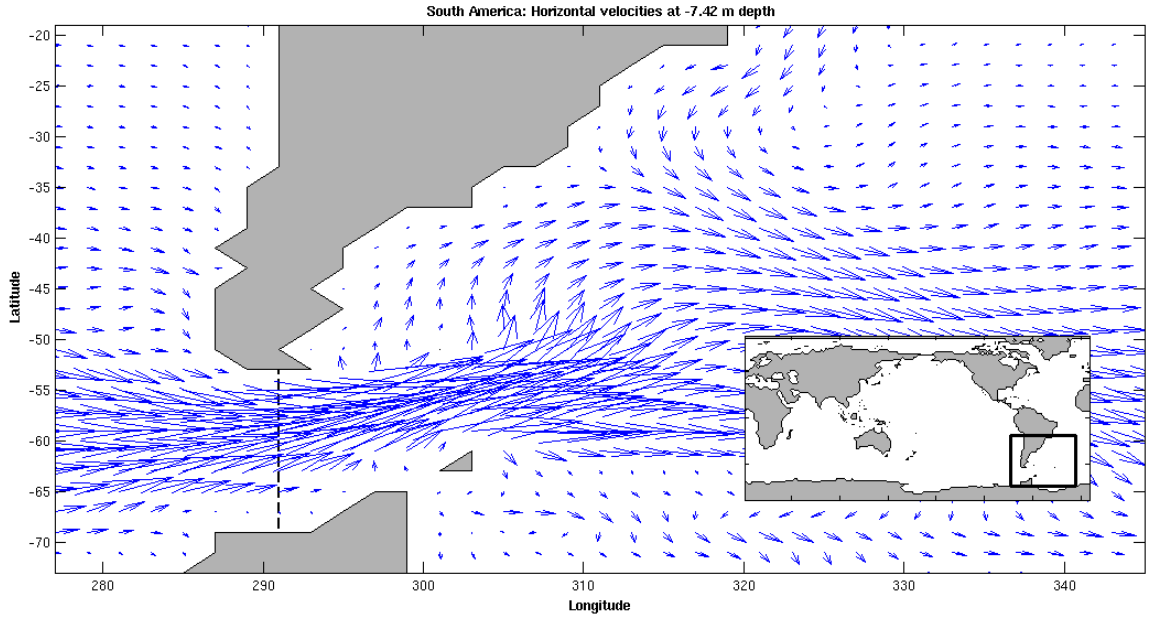

(b)

Figure 4.9: Surface velocities in (a) Atlantic and (b) South Atlantic/ACC. (c) is Figure from *Lumpkin and Johnson* (2013): Mean current speeds from near-surface drifter data with streamlines (Atlantic region is cut out from an originally global map).

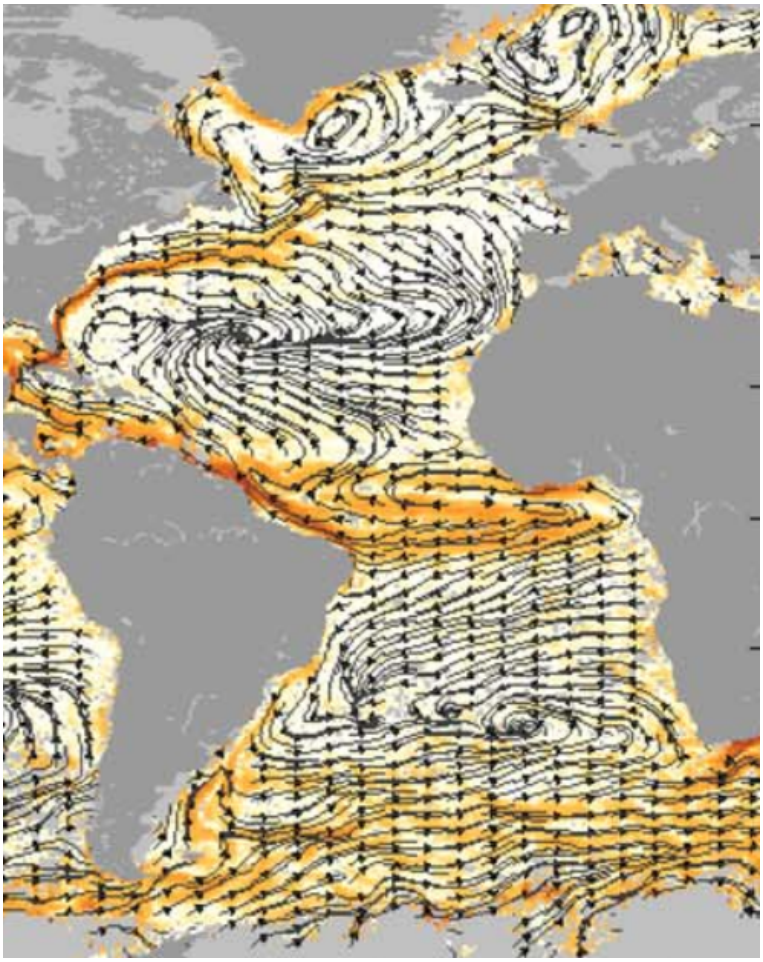

(c)

Figure 4.9: (continued)

sage to be around 134 Sv (*Cunningham et al.*, 2003), and are generally conceded to be driven principally by wind (*Baker*, 1982). *Toggweiler and Samuels* (1998) also found a strong ACC ($>$ 100 Sv) through the circumpolar channel in the absence of winds and modest amount of mixing ($\kappa_v \sim 0.5cm^2s^{-1}$), and suggested this was due to the ACC separating the cold water around Antarctica and the warmer water in the interior. Vertical mixing then depresses the isotherms in the interior, and these density differences are then able to drive a strong eastward flow through thermal wind balance. An other possible reason this strong ACC occurs in the absence of wind, is that the model resolution excludes islands that normally would distort the flow.

In the Pacific Ocean (Fig. 4.10a) there is a westward flow at and near the equator

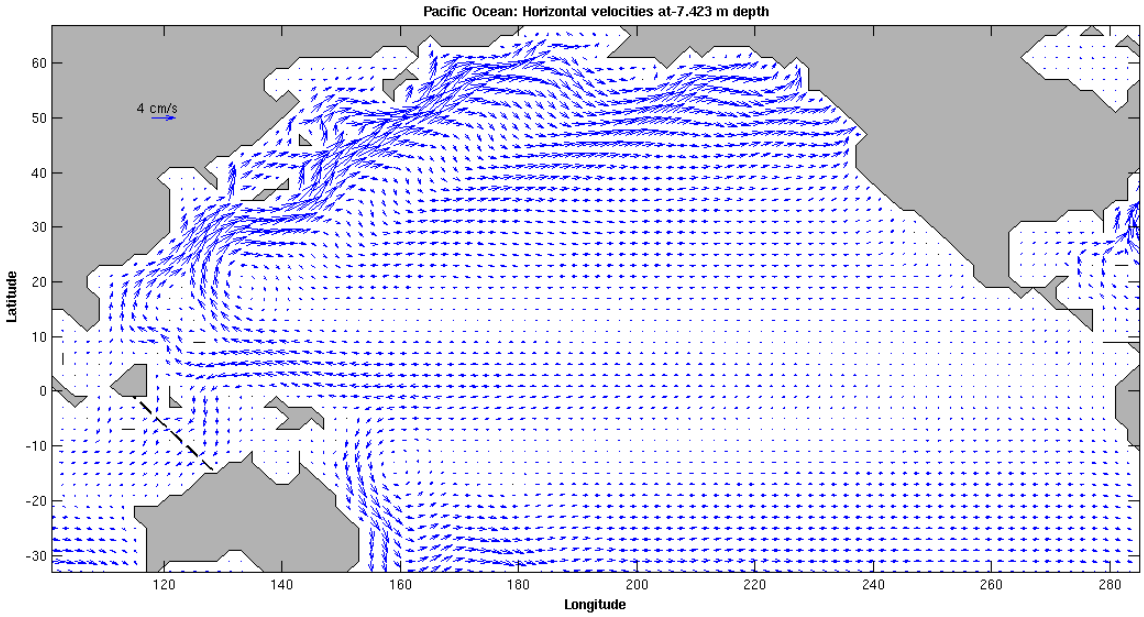

(a)

Figure 4.10: Surface velocities (a) in Pacific Ocean and (b) around South Africa/Agulhas current.

which separates when encountering the western boundary. Some of the flow enters the Indian Ocean, while the rest continues north, losing mass to an interior eastward flow. Calculation of the transport in the Indonesian Throughflow (dashed line in Fig. 4.10a) gives about 14 Sv, which is acceptable when compared to observations (*Sprintall et al.*, 2009).

After entering the Indian Ocean north of Australia the flow moves westward and reaches the eastern side of Africa, before turning southwards forming the Agulhas current, see Figure 4.10b. The Agulhas runs past the tip of South Africa, then turns back into the ACC and the Indian Ocean, known as the Agulhas Retroflection. Due to instabilities in this area intense mesoscale eddies are known to form at the eastern boundary of the South Atlantic, transporting heat from the Indian to the South Atlantic Ocean (*Olson and Evans*, 1986), called "the warm water" path. The importance of this path concerning the origin of waters that eventually form deep water in the North Atlantic (NADW) is uncertain, due to temporally unstable eddy-scale features constituting the transport (*Macdonald and Wunsch*, 1996).

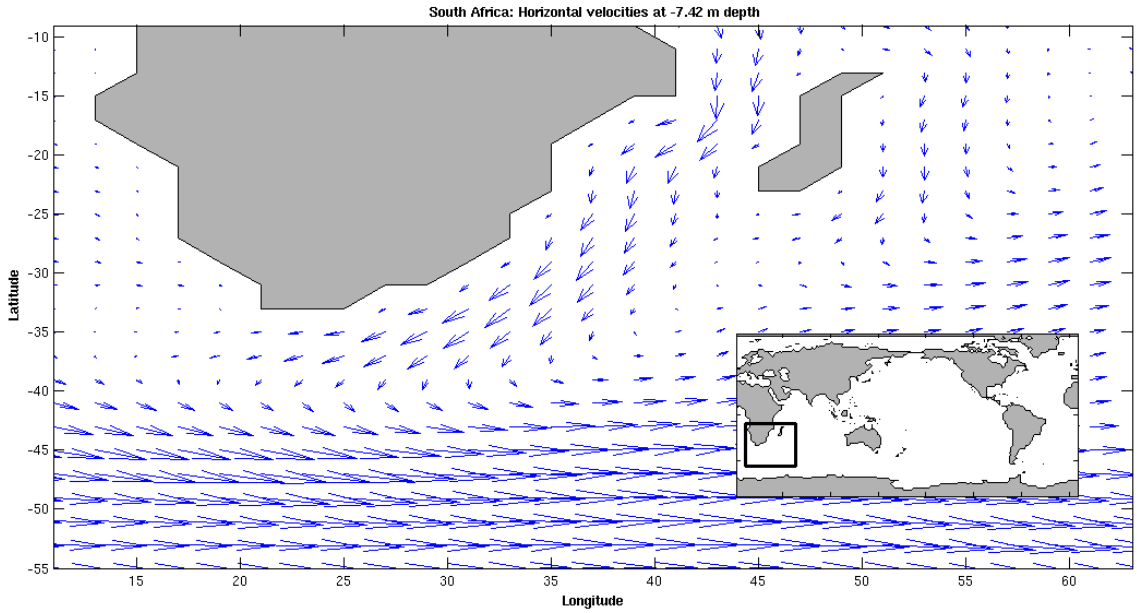

(b)

Figure 4.10: (continued)

4.2.2 Intermediate-depth circulation

As seen from the surface horizontal velocities, water is transported into the Nordic Seas from the North Atlantic. Where does this water go? At some level there must be a return flow, balancing this mass source at the surface. Figure 4.11b shows the horizontal velocities at a deeper intermediate level, and we see here a return flow from the Nordic Seas into the North Atlantic east of Iceland carrying denser waters, being steered around the coast of Greenland, forming a cyclonic rotation in the northern North Atlantic. A northward flowing western boundary current now extends all the way from Drake Passage into the North Atlantic.

In the Pacific (Fig. 4.11c) sinking in the above layers at the northeastern boundary, and upwelling below, which also is reflected in the temperature distribution in Fig. 4.1a, yields a mass flux into the interior. *Marotzke* (1997) also obtained downwelling over upwelling near the eastern boundary, thus giving an interior flow with two zero-crossings of zonal velocity (Fig. 2.6). The flow continues westward, and splits when meeting the continent. This leads to a southward flowing western boundary current, meeting up with the northward flowing western boundary current from the equator, giving rise to a relative strong flow into the Indian Ocean. At these depths some of the warmer Indian Ocean water continues around Cape

Agulhas and flows westward into the South Atlantic, where it combines with the northward flow in the Atlantic western boundary current, see Fig. 4.11a.

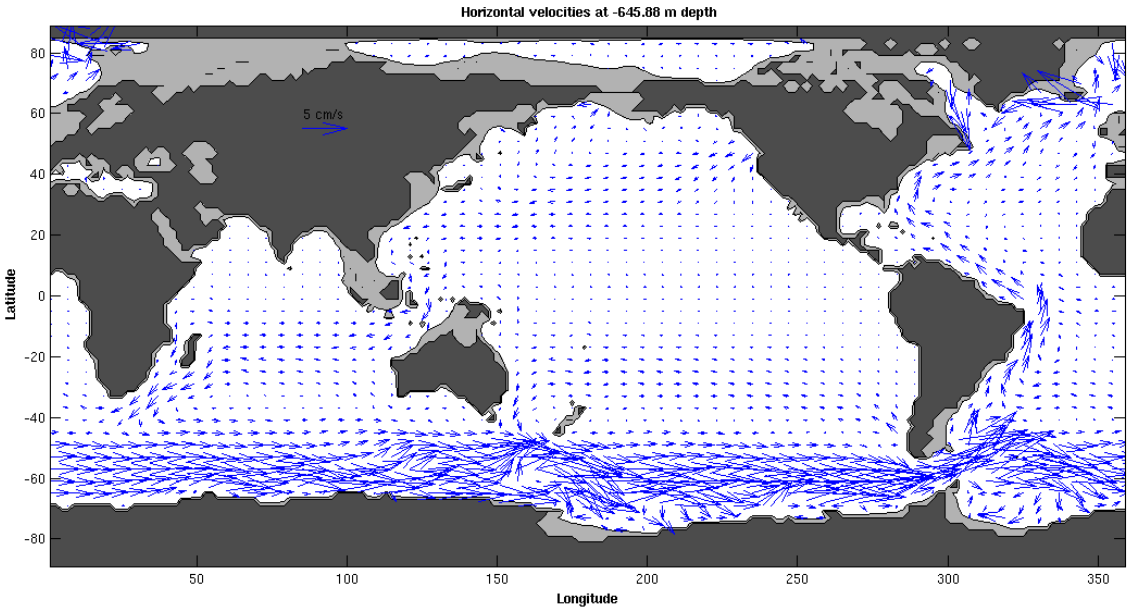

(a)

Figure 4.11: Velocities at intermediate depth in (a) global ocean, (b) Atlantic Ocean and (c) Pacific Ocean.

4.2.3 Abyssal circulation

In the abyssal regions, see Fig. 4.11a, the flow is weaker. The connection between different ocean basins is in large part blocked by topography, except in the Southern ocean. Around the southwestern Atlantic, deep waters from the north combine with the deep waters of the Weddell gyre region and water flowing through Drake Passage. This deep flow continues eastward, with inflow into the western sides of the Indian Ocean - and Pacific Ocean, see Fig. 4.11b.

Deep water formation is expected to occur in the Labrador sea and in the Nordic sea (*Marshall and Schott*, 1999). In Figure 4.12a we see a sinking region in the Labrador Sea and a deep western boundary current carrying North Atlantic deep water southward along the eastern margin of North America, with the strongest horizontal velocities near the source. Upwelling is mainly near the boundaries, and in the variable bottom topography around Drake Passage.

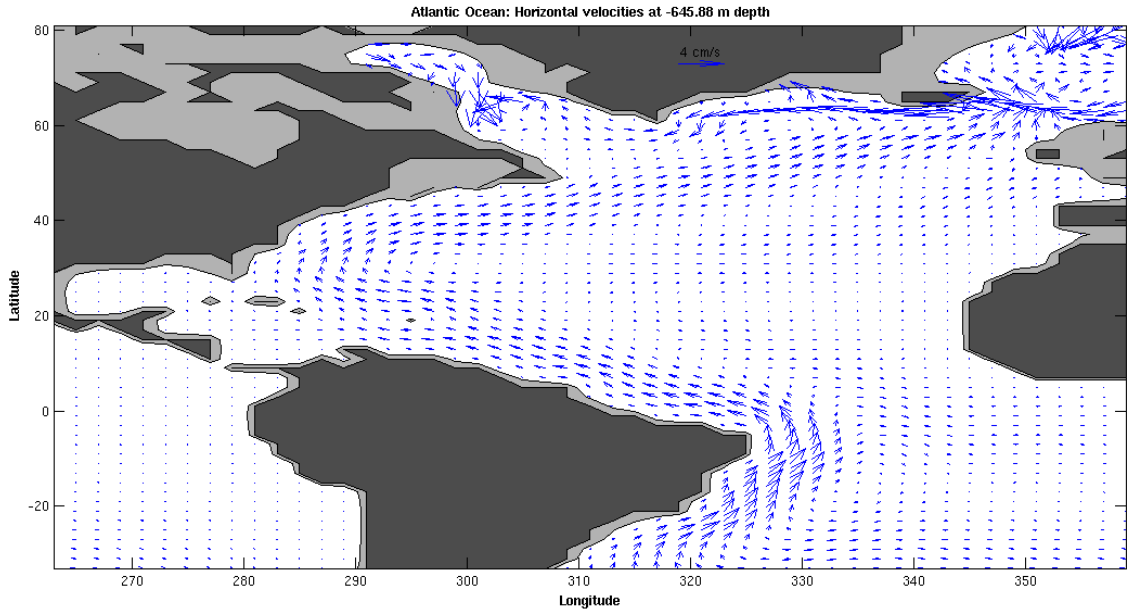
Atlantic Ocean: Horizontal velocities at -645.88 m depth
4 cm/s
Latitude
Longitude
80
60
40
20
0
-20
270
280
290
300
310
320
330
340
350

(b)

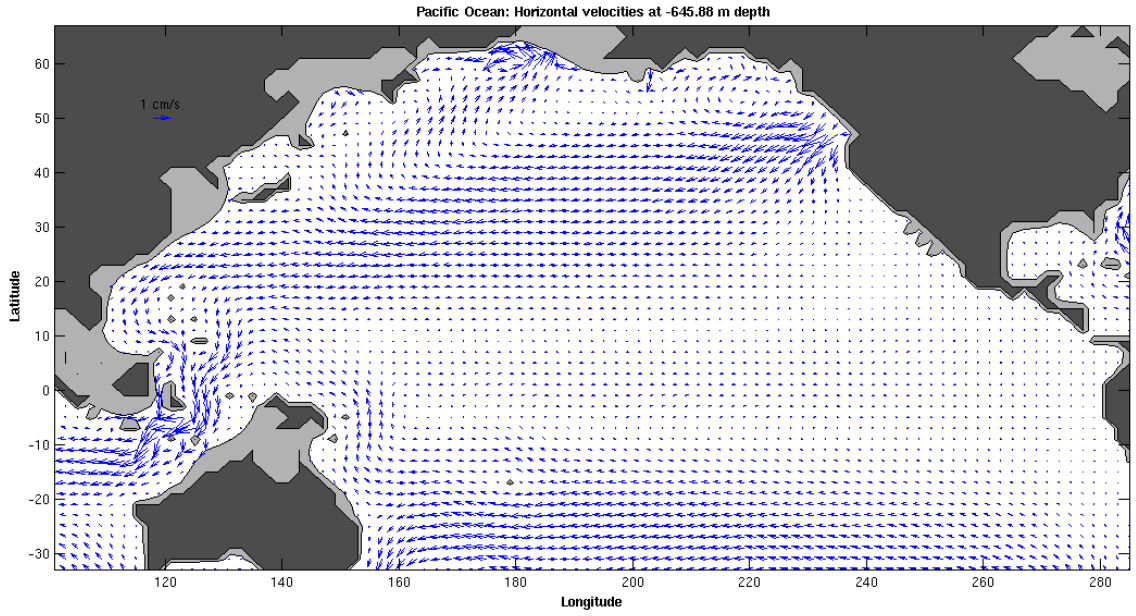
Pacific Ocean: Horizontal velocities at -645.88 m depth
1 cm/s
Latitude
Longitude
60
50
40
30
20
10
0
-10
-20
-30
120
140
160
180
200
220
240
260
280

(c)

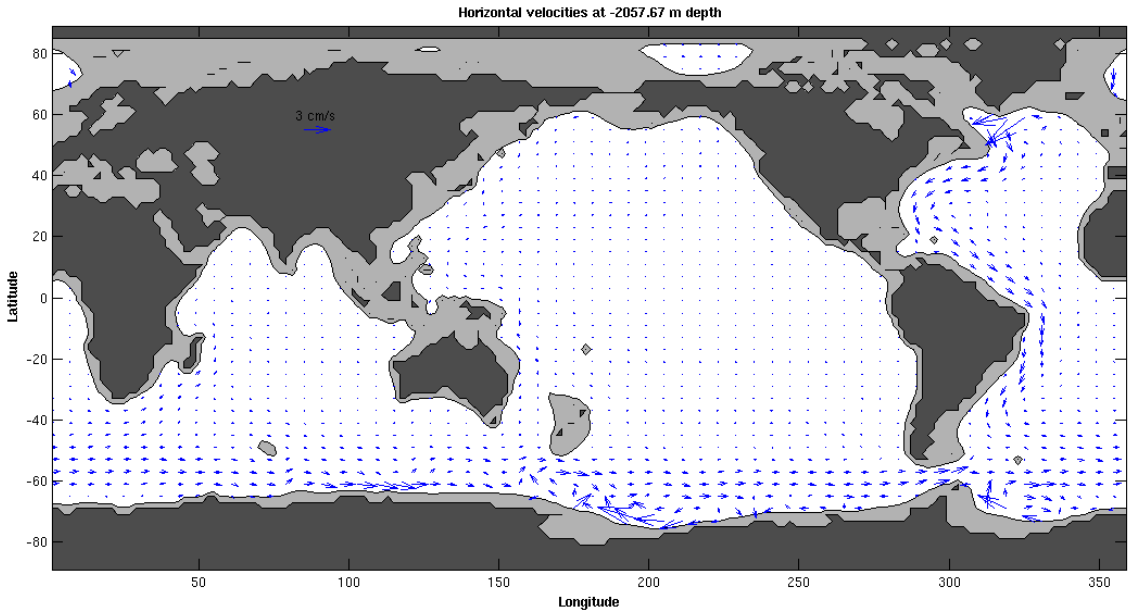

(a)

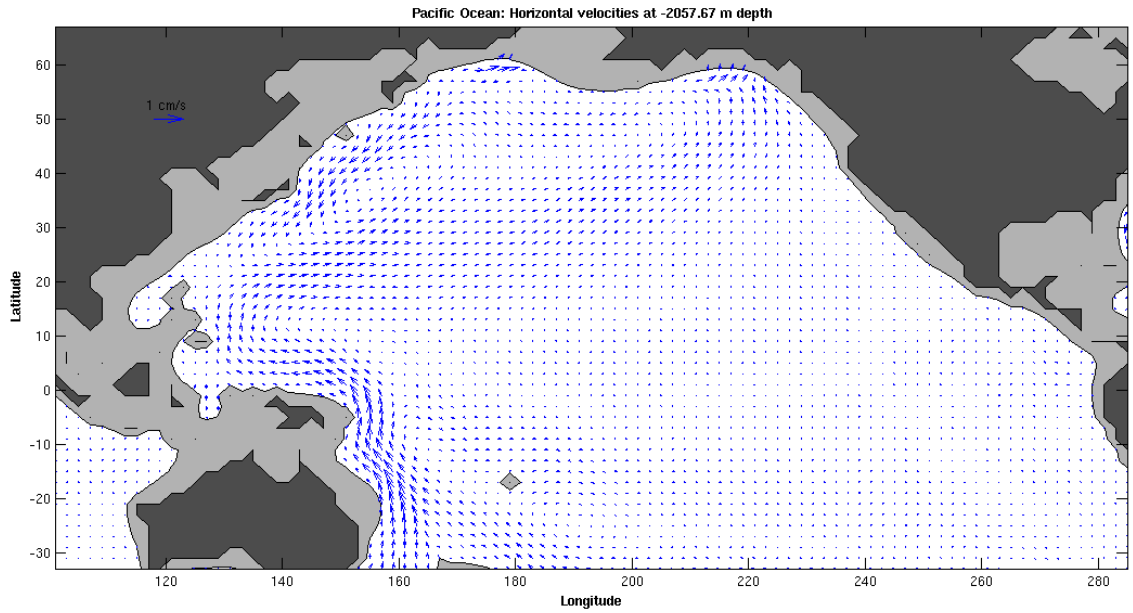

(b)

Figure 4.11: Abyssal velocities at around 2000 m in (a) global ocean and (b) Pacific Ocean.

At even deeper levels, Fig. 4.13a, dense water formed in the Antarctic move north-

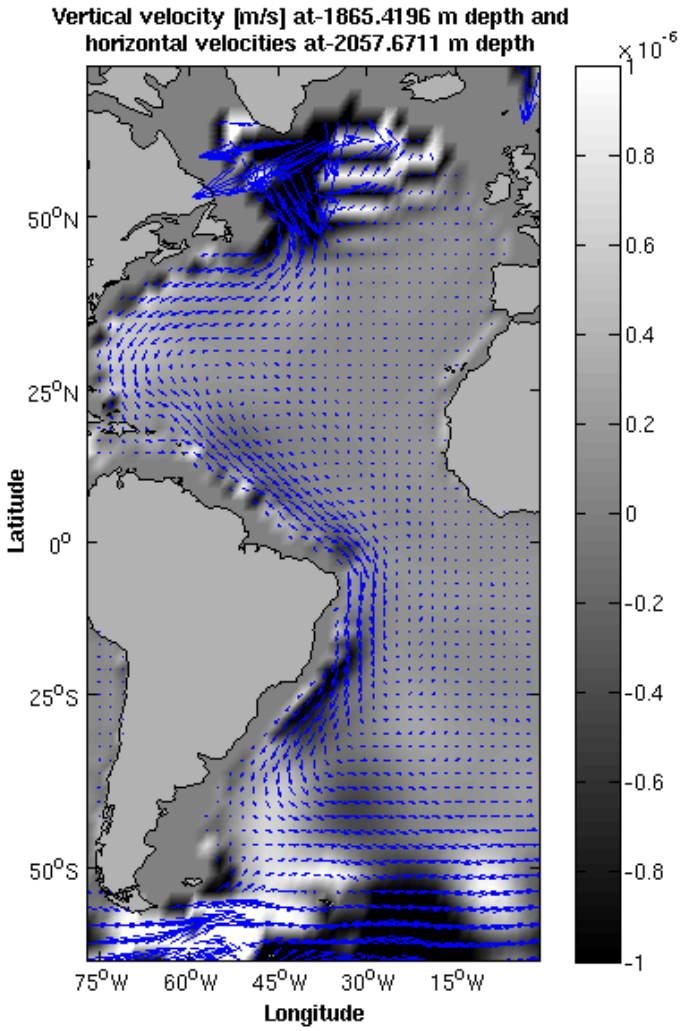

(a)

Figure 4.12: Vertical velocities at around 1900 m depth in the Atlantic Ocean. Superimposed are the horizontal velocities at around 2100 m.

wards, eventually flowing up along the western side of Africa and into the tropical and subtropical latitudes in the North Atlantic. The Greenland-Scotland ridge contains channels (not resolved in our model), such as the Denmark Strait and the Faroe Bank channel, where dense water may flow through and form North Atlantic deep water ((*Talley et al.*, 2011),(*Mauritzen*, 1996)).

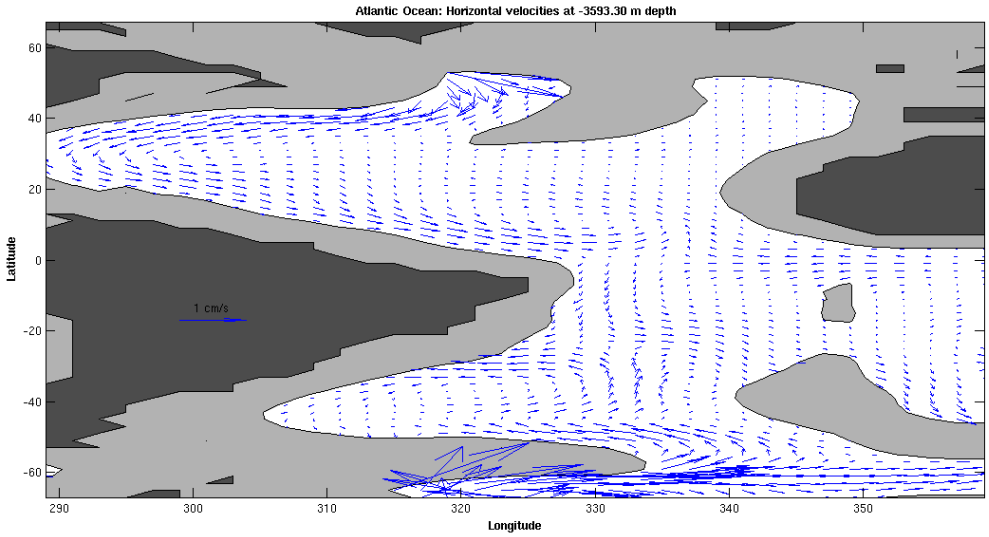

(a)

Figure 4.13: Abyssal velocities in Atlantic Ocean at around 3500 m.

4.3 Meridional overturning transport

By integrating the meridional flow zonally and vertically, see section 2.4.3, the global overturning streamfunction may be found. The overturning circulation is in this simulation solely driven by buoyancy forcing and mixing, but as has been emphasized before, the tides and winds have an indirect effect in that it enables there to a be an eddy diffusivity larger than the molecular one.

Two global-scale counterrotating cells are dominant (Fig. 4.14), and their magnitude is about the same with 29 Sv at 49°N and 31 Sv at 65°S. In the Southern Ocean the densest deep water is formed, principally in the Ross and Weddell Sea, and this dense water continues northward into the Atlantic, the Pacific and the Indian ocean, as seen in the previous section, where it is transformed to less dense water by diapycnal mixing.

Examining the Atlantic Ocean and the Indo Pacific (Indian and Pacific ocean) separately, see Fig. 4.15, we see that the upper cell is mostly associated with the Atlantic overturning, but unlike the global average, this is not a closed loop. There is some overflow of dense water from the Nordic Seas into the North Atlantic, recall Fig. 4.2f, and most of the deep sinking occurs in the latitude range of the Labrador Sea, as have been seen in previous figures.

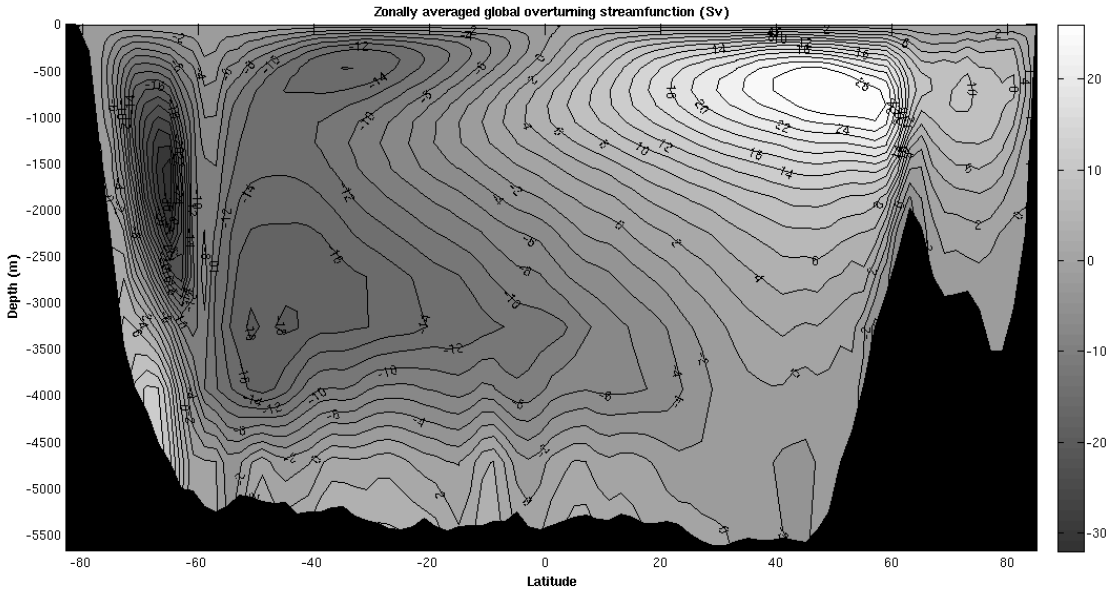

(a)

Figure 4.14: Zonally averaged global overturning streamfunction. Contour interval is a fixed volume flux of 2 Sv ($2 \times 10^6 m^3 s^{-1}$). Positive (negative) values of the streamfunction, ψ, indicate a clockwise (counterclockwise) circulation.

About 11 Sv of the deep water formed by convection in the North Atlantic travels across the equator and into the Southern Ocean. Beneath the NADW there is Antarctic bottom water inflow, about 2 Sv, originating south of the ACC that is reaching the tropical and subtropical latitudes. Features such as a western intensified boundary current are not evident, but as we have seen, the boundary currents dominate the mass flux and are an important part of the meridional overturning circulation.

In the Indo Pacific (Fig. 4.15b) there is a deep water inflow in the depth range 1700-4500m, transformed by vertical mixing into thermocline- and surface waters. In the northern hemisphere, a clockwise overturning cell is seen, more shallow than in the Atlantic, with water upwelling near the equator.

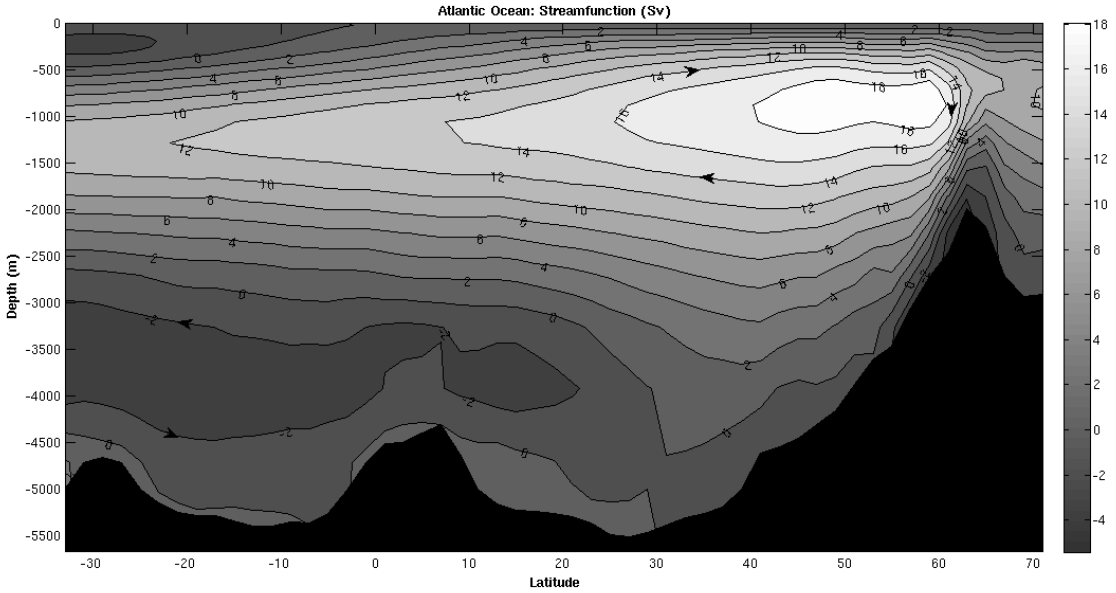

(a) Atlantic ocean: Maximum overturning (at about 1000 m depth and 50°N) is 19.5 Sv, and the outflow at −33°S is 11 Sv.

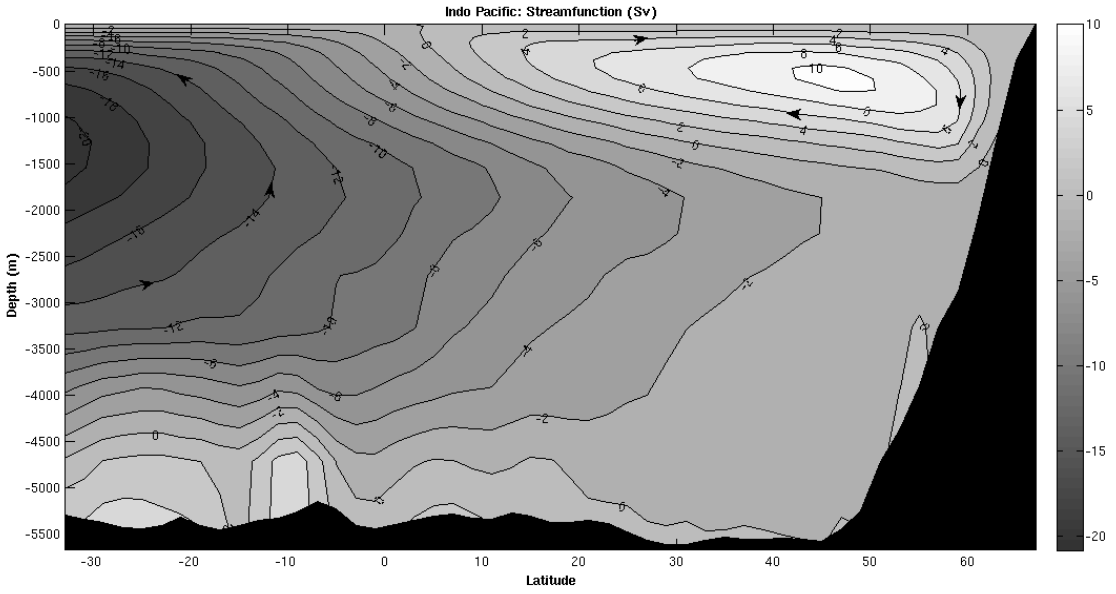

(b) Pacific ocean: Maximum overturning (at about 500 m depth and 47°N) is 10.3 Sv, and this upwells before reaching the equator.

Figure 4.15: Stream function of the zonally integrated overturning circulation in (a) the Atlantic Ocean and (b) the Indo Pacific. Contour interval is a fixed volume flux of 2 Sv ($2 \times 10^6 m^3 s^{-1}$). Positive (negative) values of the streamfunction, ψ, indicate a clockwise (counterclockwise) circulation.

Chapter 5

Summary and discussion

5.1 Comparing model results with theory and observations

In the abyss, water is transported along the western boundary. This is consistent with Stommel and Arons theory (section 2.2.1.2) and the linear thermocline theory (section 2.3). Though, in the latter the motion is confined to the upper ocean, due to its linear thermocline assumption. However, upwelling occurs mainly near the western boundaries. Thus, the interior flow differs from Stommel and Arons theory. A small recirculation gyre, though, is seen in the vicinity of the deep water source (Fig. 4.12a). Due to the meridional temperature gradient imposed, and the small vertical velocities in the interior, the surface flow is eastward. With westward flow below (Fig.4.3c and Fig4.3d), this resembles the vertical structure of the interior flow in the linear model.

Since we have neglected wind, the water filling the deep ocean can only return up to the sea surface through diapycnal mixing (section 2.2.2.1). Observations support stronger mixing near rough bottom topography and boundaries (Figure 2.3) and, as already said, this is reflected in the model results.

The thermocline of the water is at around 1000 m, but stratification also exists in the abyssal waters, though much weaker. Several previous studies have examined what is determining the ocean stratification. The importance of eddies has been studied by *Marshall et al.* (2002) and the effects of wind, diffusion and geometry by *Vallis* (2000). Deep stratification was suggested by *Vallis* (2000) to be a consequence of having an open channel, (e.g. representing Drake Passage).

An estimation of the mean global overturning over a decadal period of observa-

tions has been performed by *Lumpkin and Speer* (2007) (their Fig. 2). They find a clockwise circulation in the upper Southern Ocean, opposite to our result (Fig. 4.14). The main reason for this discrepancy is the wind. The zonal wind stress induces upwelling polewards of the surface wind maximum and downwelling on the equatorward side (section 2.2.3). Along these tilted density surfaces intermediate water may return to the surface in nearly adiabatic pathways. *Marshall and Schott* (1999) suggest that this Southern Ocean upwelling is important to the closure of the meridional circulation, since it enables water to return to the surface without invoking large thermocline diffusivities. Since wind is not included in our model, this upper level cell is not seen and the deep water return to the surface by other mechanisms, and as seen by Fig. 4.8b, mainly near the western boundaries.

If we compare the overturning in the Atlantic Ocean (Fig. 4.15a) to Figure 2.9 we see that the strength and location, about 1000 m depth and 50°N, of the overturning is approximately the same. The neglect of the direct wind influence give some differences in the upper hundred meters.

The connection between different basins is as follows; about 19 Sv sinks in the Labrador Sea fed by some overflow of dense water from the Nordic Seas. This is similar in strength compared to other estimates, see Fig.2.9. 11 Sv transverse the whole meridional extent of the Atlantic Ocean, eventually entering into the ACC. There is inflow of deep water into the western sides of the Pacific and the Indian Ocean, upwelling mainly along the western boundary, before reentering the ACC as surface and intermediate water. Figure 5.1a shows a schematic of the global overturning circulation inferred using inverse techniques incorporating observations. The main pathways of global ocean circulation contain very similar features to our model.

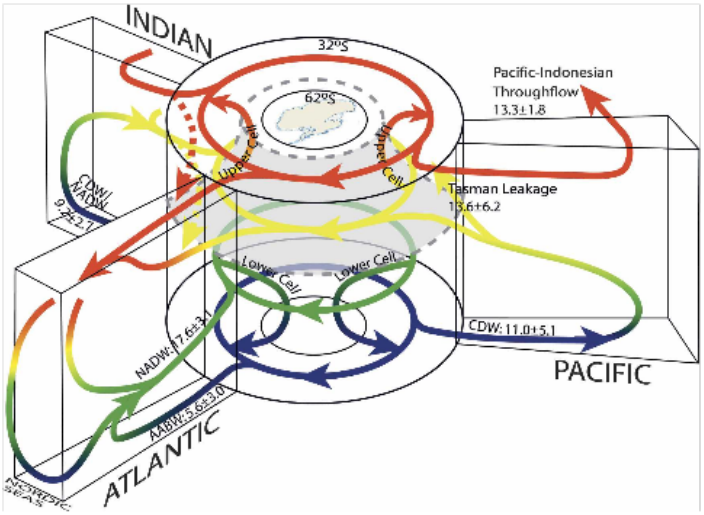

(a)

Figure 5.1: Figure from *Lumpkin and Speer* (2007): Schematic of global overturning circulation. Format adapted from *Schmitz* (1996).

5.2 Model shortcomings

The realistic strength of the meridional overturning circulation in the absence of winds, suggest that the overturning is primarily governed by thermal forcing and mixing, while winds mainly impact the upper ocean circulation. But, the model is not perfect. Even though it simulates many realistic features of the large-scale ocean circulation, it has shortcomings that, if included, would have affected the result.

5.2.1 Resolution

There is several reasons why increasing the model resolution may give a different result. First, as we have discussed previously, this may yield more pronounced eastern surface boundary currents (section 2.4) that would inhibit some of the sinking of water along the eastern boundary. Due to less sinking, the upper eastern boundary water is more stratified. The change of surface circulation and stratification may impact deep water formation rates and sites.

Second, properly resolved fracture zones in ridges would probably result in deeper dense overflows from the Nordic Seas, thereby influencing where deep water formation occurs. The region where most of the NADW formation occurs may shift

from the Labrador Sea to the Nordic Seas.

Third, the strength of the ACC would probably be reduced by including islands and topography, thereby changing its flow pattern. It would be interesting to see how this would affect the global ocean circulation.

5.2.2 Salinity and wind

The neglect of salinity is also an error of importance, particularly in high latitudes. The cycling of fresh water between the ocean and atmosphere through evaporation and precipitation affect the density of water in different locations. Brine rejection from sea ice increase the density of water, while net fresh water input at higher latitudes reduces the density, being in direct opposition to the thermal forcing, and therefore could influence the overturning rates and locations of convection.

Indirect effects of wind, contributing to the breaking of internal waves and turbulent mixing, is included in the parameterization of thermal diffusion. But, Ekman transport and gyres are excluded. From the model results we see that this provides a mean surface circulation that differs from what is observed.

Chapter 6

Conclusions

On the basis of the theory and results previously discussed, the most important conclusions are summarized in the following bullet points:

- Our model simulates vertical velocities mainly near the boundaries, with upwelling on the western side, consistent with the linear thermocline model, and observations suggesting stronger mixing near the boundaries.
- Deep water formation was found in the Antarctic region, the Nordic Seas and the North Atlantic, with the largest sinking in the Labrador Sea. These are convection sites supported by observations. As predicted by Stommel and Arons theory, the model simulates a southward moving western intensified deep flow in the Atlantic, but the interior flow differs due to their assumption of uniform upwelling.
- An interesting result is that the thermally driven numerical ocean model produce realistic overturning rates. In the Atlantic, there is an overturning rate of about 19 Sv where 11 Sv is transported into the Southern Ocean.
- Our model simulates many of the important currents in the world. Both the strength of the Indonesian Throughflow and the ACC are realistic and comparable to observations. But, especially for the ACC, the question is if this happens for the right reasons.

Appendix A

Model parameters

Continuous equation parameters

&PARM01
sRef = 24*35.,
no_slip_sides=.TRUE.,
no_slip_bottom=.TRUE.,
viscAr=1.E-4,
viscAhGrid=0.1, (Grid dependent lateral eddy viscosity)
diffKhT=500.,
diffKrT=1.E-4,
diffKhS=0.,
diffKrS=0.,
rhonil=1035.,
rhoConstFresh=1000.,
eosType = 'JMD95Z',
ivdc_kappa=100.,
rigidLid=.FALSE.,
implicitFreeSurface=.TRUE.,
implicitViscosity=.TRUE.,
implicitDiffusion=.TRUE.,
allowFreezing=.FALSE.,
tempAdvScheme = 33,
StaggerTimeStep = .TRUE.,
useRealFreshWaterFlux=.FALSE.,
useCDscheme=.FALSE.,
hFacInf=0.1,
hFacSup=5.,

hFacMin=0.3,
hFacMinDr=50.,
# set precision of data files
readBinaryPrec=32,
writeBinaryPrec=32,

Elliptic solver parameters

&PARM02
cg2dMaxIters=500,
cg2dTargetResidual=1.E-10,

Time stepping parameters

&PARM03
# 1000 years of integration will yield a reasonable flow field
startTime = 0.,
endTime = 31536000000.,
deltaT= 1800.,
abEps = 0.1,
cAdjFreq=0.,
pChkptFreq= 0.,
dumpFreq= 1.5768E9,
taveFreq= 1.5768E9,
monitorFreq= 31536000.,
# 1 months restoring timescale for temperature
tauThetaClimRelax= 2592000.,
tauSaltClimRelax = 0.,
periodicExternalForcing=.FALSE.,

Gridding parameters

&PARM04
usingSphericalPolarGrid=.TRUE.,
delR= 14.8461, 17.7881, 21.3130, 25.5365, 30.5969, 36.6601, 43.9247,
52.6290, 63.0581, 75.5539, 90.5259, 108.4648, 129.9585, 155.7114,

186.5677, 223.5385, 267.8356, 320.9107, 384.5033, 460.6977, 551.9909,
661.3751, 792.4352, 949.4666,
ygOrigin=-90.,
dySpacing=2.,
dxSpacing=2.,

Input datasets

&PARM05
bathyFile= 'smooth_bathy_2deg_wall.bin',
hydrogThetaFile= 'init_temp.bin',
thetaClimFile= 'zonal_sst_2deg_wall.bin',

Bibliography

Baker, D. J. (1982), A note on Sverdrup balance in the Southern Ocean, *J. Mar. Res*, *40*, 21–26.

Broström, G. (2008- unpublished results).

Cunningham, S. A., S. G. Alderson, B. A. King, and M. A. Brandon (2003), Transport and variability of the Antarctic Circumpolar Current in Drake Passage, *Journal of Geophysical Research: Oceans (1978–2012)*, *108*(C5).

Ghil, M. (2002), Natural climate variability, *Encyclopedia of Global Environmental Change. John Wiley and Sons, Chichester*.

Holton, J. R. (2004), *An introduction to dynamic meteorology*, Elsevier Academic Press.

Huck, T., and G. Vallis (2001), Linear stability analysis of the three-dimensional thermally-driven ocean circulation: application to interdecadal oscillations, *Tellus A*, *53*(4), 526–545.

LaCasce, J. H. (2004), Diffusivity and viscosity dependence in the linear thermocline, *J. of Marin Res.*

LaCasce, J. H. (2012), Surface quasigeostrophic solutions and baroclinic modes with exponential stratification, *J. Phys. Oceanogr.*, *42*(4), 569–580.

LaCasce, J. H., and P. E. Isachsen (2010), The linear models of the ACC, *Progress in Oceanography*, *84*(3), 139–157.

Ledwell, J., and A. Bratkovich (1995), A tracer study of mixing in the Santa Cruz Basin, *J. Geophys. Res.: Oceans (1978–2012)*, *100*(C10), 20,681–20,704.

Ledwell, J., A. Watson, and C. Law (1993), Evidence for slow mixing across the pycnocline from an open-ocean tracer release experiment, *Nature*.

Ledwell, J., E. Montgomery, K. Polzin, L. St. Laurent, R. Schmitt, and J. Toole (2000), Evidence for enhanced mixing over rough topography in the abyssal ocean, *Nature*.

Lumpkin, R., and G. C. Johnson (2013), Global ocean surface velocities from drifters: Mean, variance, El Niño-Southern Oscillation response, and seasonal cycle, *J. Geophys. Res. Oceans*.

Lumpkin, R., and K. Speer (2007), Global ocean meridional overturning, *J. Phys. Oceanogr.*

Macdonald, A. M., and C. Wunsch (1996), An estimate of global ocean circulation and heat fluxes, *Nature*, *382*(6590), 436–439.

Marotzke, J. (1997), Boundary mixing and the dynamics of three-dimensional thermohaline circulation, *J. Phys. Oceanogr.*

Marshall, J., and F. Schott (1999), Open-ocean convection: Observations, theory, and models, *Reviews of Geophysics*, *37*(1), 1–64.

Marshall, J., H. Jones, R. Karsten, and R. Wardle (2002), Can eddies set ocean stratification, *J. Phys. Oceanogr.*

Mauritzen, C. (1996), Production of dense overflow waters feeding the north atlantic across the greenland-scotland ridge. part 1: Evidence for a revised circulation scheme, *Deep-Sea Res. Part I: Oceanographic Research Papers*, *43*(6), 769–806.

Mauritzen, C., K. L. Polzin, M. S. McCartney, R. C. Millard, and D. E. West-Mack (2002), Evidence in hydrography and density fine structure for enhanced vertical mixing over the Mid-Atlantic Ridge in the western Atlantic, *J. Geophys. Res.: Oceans (1978–2012)*, *107*(C10), 11–1.

MITgcm (2014).

Munk, W. (1966), Abyssal recipes, *Deep-Sea Res.*

Munk, W., and C. Wunsch (1998), Abyssal recipes ii: Energetics of tidal and wind mixing, *Deep-Sea Res.*

Nowlin, W. D., and J. M. Klinck (1986), The physics of the Antarctic Circumpolar Current, *Reviews of Geophysics*, *24*(3), 469–491.

Nowlin Jr, W. D., T. Whitworth III, and R. D. Pillsbury (1977), Structure and transport of the Antarctic Circumpolar Current at Drake Passage from short-term measurements, *J. Phys. Oceanogr.*, *7*(6), 788–802.

Olson, D. B., and R. H. Evans (1986), Rings of the Agulhas current, *Deep-Sea Res.*

Park, Y.-G. (2006), Dependence of an eastern boundary current on the horizontal resolution in thermally driven circulations, *J. Geophys. Res.*

Pedlosky, J. (1969), Linear theory of the circulation of a stratified ocean, *J. Fluid Mech.*

Pedlosky, J. (1996), *Ocean circulation theory*, Springer-Verlag.

Samelson, R. (2011), *The theory of large-scale ocean circulation*, Cambridge University Press.

Schmitz, W. J. (1996), On the World Ocean circulation. Vol. II: The Pacific and Indian Oceans/ A global update, *Tech. rep.*, Woods Hole Oceanographic Institute.

Sprintall, J., S. E. Wijffels, R. Molcard, and I. Jaya (2009), Direct estimates of the Indonesian Throughflow entering the Indian Ocean: 2004–2006, *J. Geophys. Res.: Oceans (1978–2012)*, *114*(C7).

Stammer, D., C. Wunsch, R. Giering, C. Eckert, P. Heimback, J. Marotzke, A. Adcroft, C. N. Hill, and J. Marshall (2002), Global ocean circulation during 1992-1997, estimated from ocean observations and a general circulation model, *J. Geophys. Res.*

Stommel, H., and A. Arons (1959), On the abyssal circulation of the world ocean —I. stationary planetary flow patterns on a sphere, *Deep-Sea Res.*

Talley, L., G. Pickard, W. Emery, and J. Swift (2011), *Descriptive Physical Oceanography*, Elsevier Academic Press.

Toggweiler, J. R., and R. M. Key (2003), Thermohaline circulation, *Encyclopedia of Ocean Sciences.*

Toggweiler, J. R., and B. Samuels (1998), On the ocean's large scale circulation in the limit of no vertical mixing, *J. Phys. Oceanogr.*

Vallis, G. (2000), Large-scale circulation and production of stratification: Effects of wind, geometry and diffusion, *J. Phys. Oceanogr.*

Vallis, G. (2006), *Atmospheric and oceanic fluid dynamics*, Cambridge University Press.

Winton, M. (1997), The damping effect of bottom topography on internal decadal-scale oscillations of the thermohaline circulation, *J. Phys. Oceanogr.*, *27*(1), 203–208.

Wunsch, C. (2002), Oceanography. What is the thermohaline circulation?, *Science*.

Abstract

The thermally driven large-scale ocean circulation is studied. We obtain a steady state ocean circulation by running the time-dependent, nonlinear model to equilibrium using restoring boundary conditions on surface temperature. This is simulated by MITgcm using a $2^\circ \times 2^\circ$ spherical polar grid.

We examine how this circulation relates to theories of the surface - and the abyssal circulation. These theories include the linear thermocline theory and Stommel and Arons theory.

An important factor in returning the deep water to the surface, is the diapycnal mixing. Why this is important will be discussed. The reasons why and where the deep water upwells, are well debated. We find that positive vertical velocity mainly occurs at the western boundaries, where both the currents in the abyss and at the surface are strong.

The simulated ocean circulation contains many of the observed currents in the world, like the Antarctic Circumpolar Current (ACC), the Kuroshio Current, the Agulhas Current and the Gulf Stream. In addition, the meridional overturning has a realistic strength.